






## On the Feedback Between Air-Sea Turbulent Momentum Flux and Oceanic Submesoscale Processes

Xu Chen<sup>1,2</sup> , William Dewar<sup>3,4</sup> , Eric Chassignet<sup>2,3</sup> , Mark Bourassa<sup>2,3</sup>, Steve Morey<sup>1,2</sup> , and Ganesh Gopalakrishnan<sup>5</sup> 

<sup>1</sup>School of the Environment, Florida Agricultural and Mechanical University, Tallahassee, FL, USA, <sup>2</sup>Center for Ocean-Atmospheric Prediction Studies, Florida State University, Tallahassee, FL, USA, <sup>3</sup>Department of Ocean, Atmosphere and Earth Sciences, Florida State University, Tallahassee, FL, USA, <sup>4</sup>Laboratoire de Glaciologie et Geophysique de l'Environnement, CNRS, Grenoble, France, <sup>5</sup>Scripps Institution of Oceanography, La Jolla, CA, USA

### Key Points:

- Strong reactions of wind stress and the oceanic submesoscale to each other were found
- Wind stress field is argued to be significantly affected by both submesoscale sea surface temperature gradients and surface currents
- Submesoscale-modified wind stress has the potential to change the dynamics in the upper ocean by modifying the potential vorticity distribution

### Correspondence to:

X. Chen,  
xu.chen@famu.edu

### Citation:

Chen, X., Dewar, W., Chassignet, E., Bourassa, M., Morey, S., & Gopalakrishnan, G. (2022). On the feedback between air-sea turbulent momentum flux and oceanic submesoscale processes. *Journal of Geophysical Research: Oceans*, 127, e2022JC018767. <https://doi.org/10.1029/2022JC018767>

Received 20 APR 2022  
Accepted 12 OCT 2022

**Abstract** Accurate representation of air-sea interaction is crucial to numerical prediction of the ocean, weather, and climate. Sea surface temperature (SST) gradients and surface currents in the oceanic mesoscale regime are known to have significant influence on air-sea fluxes of momentum. Studies based on high-resolution numerical models and observations reveal that SST gradients and surface currents in the submesoscale regime are much stronger than those in the mesoscale. However, the feedback between the submesoscale processes and the air-sea turbulent fluxes is not well understood. To quantitatively assess the responses between air-sea flux of momentum and submesoscale processes, a non-hydrostatic ocean model is implemented in this study. The inclusion of SST gradients and surface currents in air-sea bulk fluxes are argued to be significant for modeling accurate wind stress in the submesoscale regime. Taking both into account, this study shows that the linear relationship between wind stress curl/divergence and crosswind/downwind SST gradients existing in the mesoscale regime is not obvious in the submesoscale. Instead, a linear relationship between wind stress curl/divergence and surface current curl/divergence is revealed in the submesoscale. Furthermore, the magnitude of wind stress curl introduced by submesoscale processes is much greater than that presented by mesoscale processes. Another key finding is that tracer subduction and potential vorticity distribution in the submesoscale is susceptible to submesoscale-modified air-sea turbulent momentum flux. This study serves as a starting point in investigating the feedbacks between atmospheric and oceanic submesoscale processes.

**Plain Language Summary** Sea surface temperature (SST) gradients and surface currents can significantly influence air-sea fluxes of momentum in the mesoscale regime. In the recent decade, high-resolution numerical models and observations reveal that SST gradients and surface currents in the submesoscale regime (length scale of order 1 km) are much stronger than those in the mesoscale (length scale of order 10–100 km). But the feedback between the submesoscale processes and the air-sea turbulent fluxes is not well understood. In this study, we quantitatively assessed the responses between the air-sea flux of momentum and oceanic submesoscale processes and found the impact of including SST gradients and surface currents on air-sea bulk fluxes is significant for accurately modeling wind stress in the submesoscale regime. We also found the linear relationship between wind stress curl/divergence and crosswind/downwind SST gradients existing in the mesoscale regime is not obvious in the submesoscale. Instead, a linear relationship between wind stress curl/divergence and surface current curl/divergence is found in the submesoscale. Furthermore, the submesoscale wind stress curl is found to be much stronger (of greater magnitude) than previously identified in mesoscale studies. The strong wind stress curl in submesoscale can significantly influence tracer subduction and potential vorticity distribution, which indicates that the wind stress coupling with currents is very important for submesoscale modeling air-sea interactions and predicting the ocean, weather, and climate.

### 1. Introduction

Accurately representing wind stress is crucial for numerically simulating air-sea exchanges and marine atmospheric boundary layer (MABL) physics which are key components in ocean, weather, and climate forecasts. However, biases in air-sea fluxes have been shown to cause significant errors in large-scale forecasts (Bourassa et al., 2013; Lee et al., 2013; Moore & Renfrew, 2002; Roberts et al., 2012; Rogers, 1995; Zhang et al., 2016).

Neglecting the ocean surface currents in the wind stress calculation is one reason that has been put forward for the biases in air-sea fluxes of heat and momentum in numerical models (Chelton et al., 2004; Dawe & Thompson, 2006; Duhaut & Straub, 2006; Scott & Arbic, 2007; Seo, 2017; Seo et al., 2016; Renault, Molemaker, Gula, et al., 2016; Renault, Molemaker, McWilliams, et al., 2016; Renault, McWilliams, & Masson, 2017; Renault, McWilliams, & Penven, 2017; Renault et al., 2018, 2020; Seo et al., 2019; Wu et al., 2017; Zhai & Greatbatch, 2007). Resolving the influence of sea surface temperature (SST) (on wind speed and boundary-layer stratification) is also considered crucial in accurately modeling the air-sea fluxes (Chelton et al., 2004; Gaube et al., 2015; Hayers et al., 1989; O'Neill et al., 2010; Seo, 2017; Seo et al., 2016; Shi & Bourassa, 2019; Small et al., 2008; Spall, 2007; Strobach et al., 2022; Sullivan et al., 2020). Furthermore, with more finer-scale processes being resolved in ocean models due to the improvements in numerical techniques and computational resources, the biases of wind stress and heat flux at the air-sea interface are found to be dependent on model resolutions (Renault et al., 2018, 2020).

In mesoscale-resolved (mesoscale-resolution) forerunner studies, properly considering the influences of ocean surface currents and SST on air-sea interactions can improve the accuracy of numerical studies related to eddy energetics, ocean currents dynamics, and climate prediction (Ma et al., 2016; Renault, McWilliams, & Penven, 2017; Seo, 2017; Seo et al., 2016; Shi & Bourassa, 2019). It has also been concluded that considering mesoscale SST gradients and surface currents in the wind stress parameterization improves the modeling of the MABL (Dawe & Thompson, 2006; Deremble et al., 2013; Duhaut & Straub, 2006; Scott & Arbic, 2007; Wu et al., 2017; Zhai & Greatbatch, 2007). While mesoscale air-sea coupling and its impact on multi-scale oceanic and atmospheric dynamics are active areas of research, the submesoscale air-sea coupling is an area of growing interest as the richness of submesoscale processes emerged with the increase in resolution in both observations and numerical modeling (Bachman et al., 2017; Boccaletti et al., 2007; Capet et al., 2008; Dong et al., 2020; Fox-Kemper et al., 2008; McWilliams, 2016; Renault et al., 2018; Stamper & Taylor, 2017; Su et al., 2018; Thomas et al., 2008).

Bridging the quasi-geostrophic mesoscale (10–100 km) and small dissipation-scale (0.1–100 m) processes, the submesoscale processes feature an intermediate lateral length scale between 100 m and 10 km (McWilliams, 2016; Thomas et al., 2008). Breaking down the geostrophic balance (Charney, 1971; Scott & Arbic, 2007) and leading to secondary ageostrophic circulation, the submesoscale provides an alternative dissipation route in the ocean (Capet et al., 2008; D'Asaro et al., 2011; McWilliams, 2003, 2016; McWilliams et al., 2001). Moreover, submesoscale structures are associated with strong vertical velocity, which is usually 1–2 orders greater than what is typical in the mesoscale regime ( $10^{-4}$ – $10^{-5}$  m s<sup>-1</sup>) (Mahadevan, 2016; Mahadevan et al., 2008; Thomas et al., 2008). The strong submesoscale vertical velocities can redistribute a significant amount of buoyancy to re-stratify the upper ocean (Boccaletti et al., 2007; Capet et al., 2008; Fox-Kemper et al., 2008; McWilliams, 2016; Shi & Bourassa, 2019; Thomas et al., 2008) and influence heat exchanges (Su et al., 2018), as well as influence the transport of tracers (Stamper & Taylor, 2017; D'Asaro et al., 2018) such as nutrients and marine organisms to impact phytoplankton production and biogeochemical cycling (D'Asaro et al., 2018; Klein & Lapeyre, 2009; Lévy, Ferrari, et al., 2012; Mahadevan, 2016). In particular, CO<sub>2</sub> fluxes are limited by the transport of CO<sub>2</sub> into and out of the near surface ocean (Sabine & Tanhua, 2010), which suggests that the submesoscale processes might be critical for transporting CO<sub>2</sub> into the ocean interior and influencing the uptake rate of CO<sub>2</sub> between the ocean and atmosphere (Sarmiento et al., 1992).

In addition to the dynamical importance of the submesoscale processes, a better understanding on the feedback between wind stress and the submesoscale processes is necessary in light of the fact that the magnitudes of surface vorticity and SST gradients in the submesoscale regime are much greater than those in the mesoscale (Capet et al., 2008; Chelton et al., 2004; Fox-Kemper et al., 2008; McWilliams, 2016; Stamper & Taylor, 2017; Thomas & Ferrari, 2008; Thomas et al., 2008). In a numerical model, the contribution of SST and surface currents to the wind stress can be expressed via a bulk formula (Fairall et al., 2003; Kara et al., 2000), that is,

$$\tau = \rho C_D \left( T_{\text{atm}}, \text{SST}, |\bar{U} - \bar{U}_{\text{sfc}}| \right) \left( \bar{U} - \bar{U}_{\text{sfc}} \right) |\bar{U} - \bar{U}_{\text{sfc}}| \quad (1)$$

where  $\tau$  is the wind stress,  $\rho$  is air density,  $C_D$  is the drag coefficient which is also a function of SST, atmospheric potential temperature  $T_{\text{atm}}$  (10-m height), surface current velocity (vector  $U_{\text{sfc}}$ ), and wind velocity (vector  $U$ ) (10-m height). Although surface waves are a factor influencing the drag coefficient, waves are not considered in Equation 1 because our numerical study does not include a wave component. In this study, wind speed, air

humidity, and air temperature are prescribed as constants such that wind stress has no dependencies on them. Thus, we can focus on the wind stress's modulation merely induced by the ocean (SST and surface current), which can be expressed as Equation 2:

$$\delta\tau = \frac{\partial\tau}{\partial\text{SST}}\delta\text{SST} + \frac{\partial\tau}{\partial\overline{U}_{\text{sfc}}}\delta\overline{U}_{\text{sfc}} \quad (2)$$

where  $\delta$  is the change. Equation 2 can be divided by the length of scale,  $L$ , to be further expanded to Equation 3

$$\begin{aligned} \frac{\delta\tau}{L} = & \rho \left( \overline{U} - \overline{U}_{\text{sfc}} \right) \left| \overline{U} - \overline{U}_{\text{sfc}} \right| \frac{\partial C_D}{\partial\text{SST}} \frac{\delta\text{SST}}{L} + \rho \left( \overline{U} - \overline{U}_{\text{sfc}} \right) \left| \overline{U} - \overline{U}_{\text{sfc}} \right| \frac{\partial C_D}{\partial\overline{U}_{\text{sfc}}} \frac{\delta\overline{U}_{\text{sfc}}}{L} \\ & + \rho C_D \frac{\partial \left[ \left( \overline{U} - \overline{U}_{\text{sfc}} \right) \left| \overline{U} - \overline{U}_{\text{sfc}} \right| \right]}{\partial\overline{U}_{\text{sfc}}} \frac{\delta\overline{U}_{\text{sfc}}}{L} \end{aligned} \quad (3)$$

Simple scale analyses of Equation 3 in the submesoscale and large scales (including mesoscale) were conducted as follows. Assuming the magnitudes of surface velocity, SST, and wind speed have no dependence on length scales, the magnitudes of  $\rho \left( \overline{U} - \overline{U}_{\text{sfc}} \right) \left| \overline{U} - \overline{U}_{\text{sfc}} \right| \frac{\partial C_D}{\partial\text{SST}}$ ,  $\rho \left( \overline{U} - \overline{U}_{\text{sfc}} \right) \left| \overline{U} - \overline{U}_{\text{sfc}} \right| \frac{\partial C_D}{\partial\overline{U}_{\text{sfc}}}$ , and  $\rho C_D \frac{\partial \left[ \left( \overline{U} - \overline{U}_{\text{sfc}} \right) \left| \overline{U} - \overline{U}_{\text{sfc}} \right| \right]}{\partial\overline{U}_{\text{sfc}}}$  in submesoscale and large scales should have no significant differences.

However, given the mesoscale length scale is of 10–100 km, which can be 10–100 times greater than that of the submesoscale (0.1–10 km) (McWilliams, 2016; Thomas, 2008), according to Equation 3, the magnitude of wind stress curl/divergence in the submesoscale has the potential to be 10–100 times greater than those in the meso- and large-scales. In the meso- and large-scale regions where the current shear and divergence are not strong, a linear relationship between wind stress curl/divergence and crosswind/downwind SST gradients has been found in observation and numerical studies (Chelton et al., 2004; Maloney & Chelton, 2006; Shi & Bourassa, 2019). The magnitude of the linear function slope is defined as coupling coefficient and has been demonstrated to have different values across distinct regions (Chelton et al., 2004; Maloney & Chelton, 2006; Spall, 2007). In large-scale, weak current shear regions ( $\text{Ro} = UL/f \ll 1$ ,  $\text{Ro}$  is Rossby number,  $U$ ,  $L$  scales of velocity and length,  $f$  planetary vorticity), SST gradients seem to be the dominating factor influencing the magnitudes of wind stress curl/divergence through the first term (I term) on the right side of Equation 3. The second (II term) and third (III term) terms are of small magnitudes because the scale of  $UL$  ( $\ll f$ ) is fairly small. However, in the submesoscale, not only can the magnitudes of SST gradients be much greater than those in the mesoscale, but the curl/divergence of surface current ( $UL \sim f$ ) can also be greater. Therefore, the II and III terms in Equation 3 in the submesoscale can be of greater magnitude than the meso- and large-scales. This is also consistent with the intuition that the strong surface current curl/divergence in submesoscale introduces strong wind stress curl/divergence with an opposite sign because of the positive correlation between the wind stress and the ocean surface current as shown in Equation 1. In Section 3.1, we strive to answer the question of whether and how much, quantitatively, the strong submesoscale SST gradients can affect the wind stress curl and divergence fields (the I term on the right side of Equation 3). Furthermore, the response of wind stress field to the submesoscale surface current curl/divergence (the II and III terms on the right side of Equation 3) is examined (Section 3.2) with the inclusion of surface currents in wind stress calculations switched on and off. These wind stress field responses in the submesoscale (Sections 3.1 and 3.2) are also compared with wind stress field responses in the mesoscale in Section 3.3. Finally, how the submesoscale-modulated wind stress field influence the ocean dynamics from the perspectives of vertical transport and potential vorticity (PV) distribution is investigated in Sections 3.4 and 3.5, respectively.

Being a conservative and active tracer related to the dynamics, the PV field is explored because its vertical transport throughout the mixed layer is vital for connecting the surface, the mixed layer, and the deep ocean (Marshall & Nurser, 1992). Negative PV injection from down-front winds is an important trigger of instability in the mixed layer (D'Asaro et al., 2011; Thomas, 2008; Thomas & Lee, 2005; Wenegrat et al., 2018). In the submesoscale regimes, which are associated with strong vertical velocities, PV surface flux has been proved (D'Asaro et al., 2011; Thomas & Lee, 2005; Wenegrat et al., 2018) to have close associations with the upper layer PV budget and air-sea interactions. Therefore, to investigate the feedback between wind stress and submesoscale features with strong SST gradients and enhanced surface vorticity, a numerical modeling study was conducted in this work to examine (a) how wind stress responds to submesoscale SST gradients and the current vorticity field

and (b) how the submesoscale-modified wind stress impacts the evolution of the submesoscale processes (vertical transports and PV distribution) in the mixed layer of the ocean.

To simulate the oceanic submesoscale processes and air-sea turbulent fluxes, this study uses a high-resolution, non-hydrostatic ocean model with an air-sea turbulent flux algorithm (Coupled Ocean-Atmosphere Response Experiment, version 3, i.e., COARE3) (Fairall et al., 2003; Kara et al., 2000) module. Although the COARE algorithm assumes a homogeneous surface condition, there is no flux parameterization appropriate for the non-homogeneous surface condition at present. In addition, Monin-Obukhov similarity theory is used on substantially non-homogeneous structures such as mesoscale frontal crossing and compares well to eddy correlation fluxes (J. Edson, personal communication, 2022). Details of the numerical experiments are described in the Section 2. Quantitative diagnostics on the response of wind stress curl/divergence to the submesoscale surface features (SST and surface currents), and how the modified wind stress field affect the upper ocean dynamics (vertical transport and PV distribution) are analyzed and discussed in Section 3. How these research findings contribute toward an expanded understanding of the submesoscale air-sea interaction and its potential influences on upper ocean dynamics are summarized in Section 4.

## 2. Numerical Experiments

A set of numerical experiments using the Massachusetts Institute of Technology general circulation model (MITgcm) are conducted to generate submesoscale processes and investigate the mutual responses between the submesoscale processes and wind stress. In the submesoscale generation experiment, the model starts and runs without wind forcing for 180 hr and then a 4 m/s uniform wind forcing is applied for an additional 24 hr. A submesoscale eddy and strong front is formed at the 204th hr in the submesoscale generation experiment. Then, contrast experiments are conducted to test two wind stress calculation schemes over the submesoscale field for 6 hr. Key diagnoses and comparisons are carried out for the 6-hr contrast experiments. For simplicity, both long-wave and shortwave radiative fluxes are switched off in these experiments.

### 2.1. Submesoscale Generation Experiment

The first objective of the numerical model is to simulate submesoscale processes. Equipped with both hydrostatic and non-hydrostatic configurations, the MITgcm can simulate phenomena ranging from small-scale to planetary scales (Marshall et al., 1997). Many previous modeling studies have implemented the MITgcm to simulate the submesoscale processes in the ocean (e.g., Bachman et al., 2017; Brannigan et al., 2015, 2017; Hamlington et al., 2014; Rosso et al., 2015). With the non-hydrostatic module used to capture the strong vertical accelerations near the surface, the submesoscale generation experiment is conducted to allow possible symmetric instabilities, a transition to baroclinic instabilities, and submesoscale eddies to occur (similar to Stamper & Taylor, 2017). The model domain consists of a flat-bottomed square box with the horizontal and vertical dimensions of 5 km and 100 m, respectively. Discretized into 50 vertical  $z$  levels and 500 horizontal grid cells in the zonal and meridional direction, the model has a uniform vertical resolution of 2 m and horizontal resolution of 10 m to resolve variabilities for horizontal spatial scale less than 5 km. Isotropic viscosity of  $1 \times 10^{-3} \text{ m}^2 \text{ s}^{-1}$  and thermal diffusivity of  $1 \times 10^{-3} \text{ m}^2 \text{ s}^{-1}$  are used in the submesoscale generation run without wind forcing (during the first 180 hr) to allow possible small-scale processes to materialize (Stamper & Taylor, 2017). While the northern and southern lateral boundaries are closed and free-slip, the western and eastern boundaries are set periodic to make the model domain a periodic channel.

The initial fields of temperature and the velocity zonal component,  $u$ , for the submesoscale generation experiment are shown in Figure 1. The initial meridional component of velocity,  $v$ , is set to zero across the domain, while the zonal velocity is geostrophically balanced with a pressure field, as indicated in Equation 4, that is,

$$-fu = \frac{1}{\rho_0} \frac{\partial P}{\partial y} \quad (4)$$

where  $f$  is Coriolis parameter,  $P$  is pressure,  $\rho_0$  is reference density, and  $u$  is the zonal component of velocity. The model is on an  $f$ -plane with Coriolis parameter  $f$  being a constant of  $8.7745 \times 10^{-5} \text{ s}^{-1}$ . A linear equation of state has been implemented in the model, as shown in Equation 5, that is,

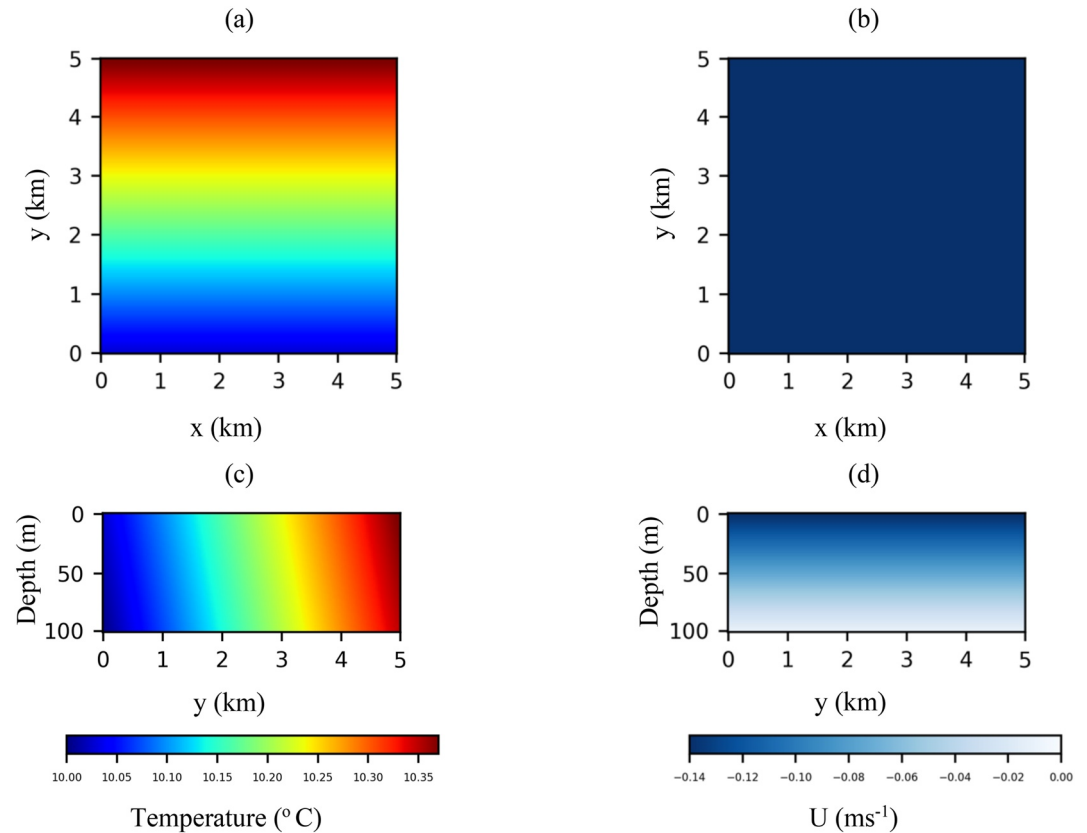


**Figure 1.** Initial temperature (left panels) and  $u$  velocity (right panels) at the surface (upper panels) and a transect of an arbitrary south-north slice (bottom panels).

$$\rho = \rho_0 [1 - \alpha (T - T_0)] \quad (5)$$

where  $\alpha$  is  $1.7 \times 10^{-4} \text{C}^{-1}$ ,  $T$  is temperature,  $\rho$  is density, and  $T_0$  and  $\rho_0$  are references for temperature and density, respectively. The salinity term is not shown in Equation 5 because it is set to a constant value (34 psu) throughout the whole domain. Substituting Equation 5 and the hydrostatic equation into Equation 4 yields to Equation 6, that is,

$$\frac{\partial u}{\partial z} = -\frac{\alpha g}{f} \frac{\partial T}{\partial y} \quad (6)$$

In Figures 1a and 1c, the warmer temperature (smaller density) at the northern sides of the channel indicates a positive temperature gradient along the  $y$  direction that balances the negative  $u$  gradient in the  $z$  direction, as shown in Figure 1d.

The magnitude of westward flow in Figure 1d reaches its maximum at the surface. The surface flow is uniform and geostrophically balanced by the meridional sea surface height gradient, which is 0 cm at the southern boundary and linearly increases to 0.64 cm at the northern boundary. The Richardson number of the initial condition is 0.25, which enables both symmetric instability and baroclinic instability to occur (Stamper & Taylor, 2017; Stone, 1966). The submesoscale generation simulation is run for 180 hr without surface forcing, in which symmetric instabilities, a transition to baroclinic instabilities, and submesoscale eddies materialize. The evolution of the surface buoyancy field shown in Figure 2 is similar to the findings of Stamper and Taylor (2017). Symmetric instability cells are observed in Figure 2b and a submesoscale eddy is formed at the 180th hr (Figure 2f). A transition between the symmetric instability and baroclinic instability is well recognized in Figures 2c and 2d.

The algorithm of COARE3, assembled in the CheapAML model (Dereemble et al., 2013), is switched on in MITgcm to introduce air-sea turbulent fluxes. It is worth noting that only the COARE3 algorithm in CheapAML

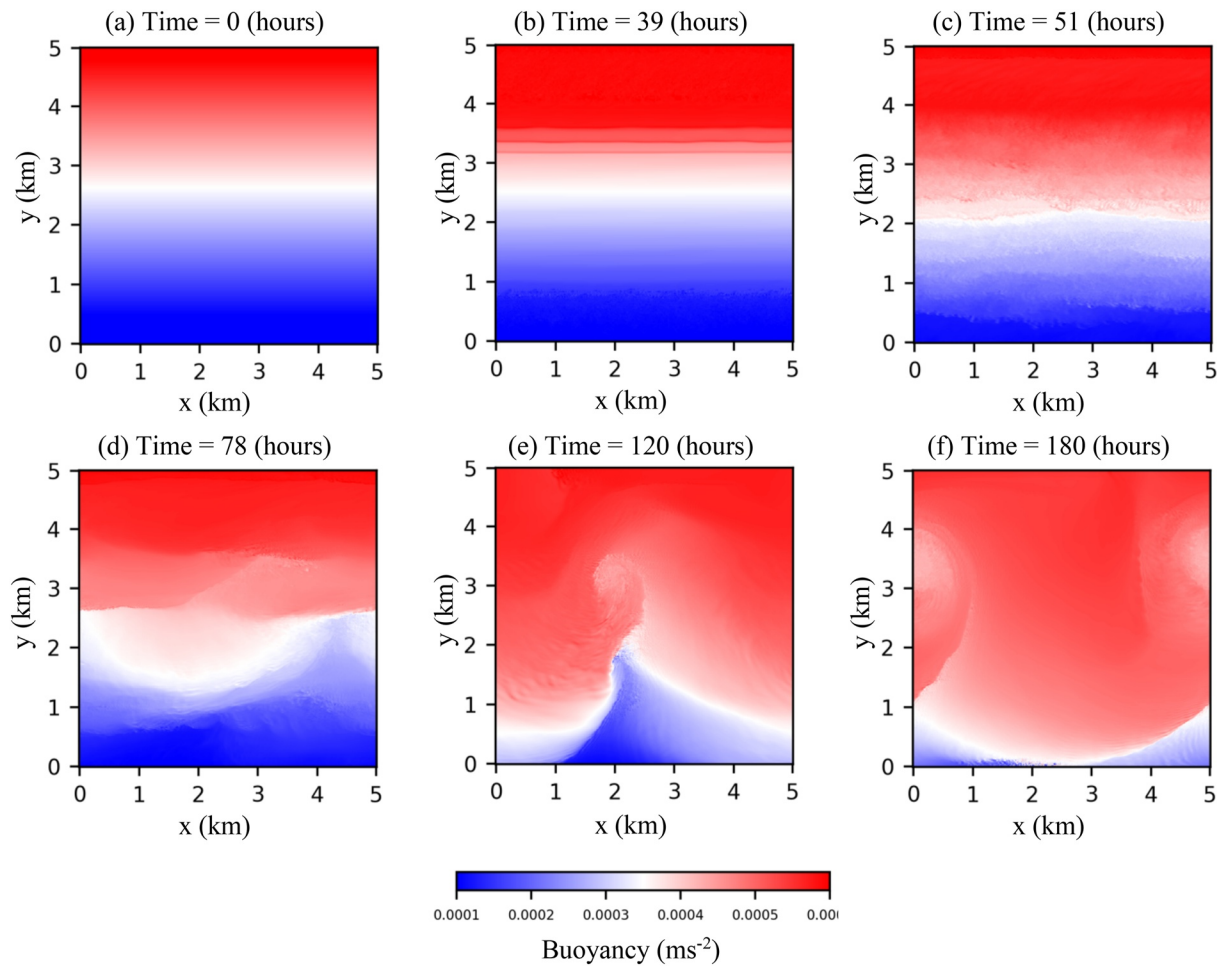


**Figure 2.** The evolution of surface buoyancy of the preliminary run.

is used and that neither the atmospheric boundary layer dynamics nor thermodynamics are switched on. While acknowledging the important role that the atmospheric boundary layer can play in air-sea interactions, we opted to keep the atmospheric boundary layer decoupled to focus on the interactions between the oceanic submesoscale processes and wind stress, rather than a more complex question in an atmospheric boundary coupled system. As mentioned earlier, after the no-forcing submesoscale generation experiment is run for 180 hr, a submesoscale eddy along with a strong front appears in Figure 2f.

Then, a uniform westward wind field of  $4 \text{ m s}^{-1}$  is applied to force the ocean model for 24 hr, during which time the wind stress is calculated according to Equation 1 with surface currents included. Air temperature at a height of 10 m is prescribed as a fixed value of  $10.2^\circ\text{C}$ , which is the average SST at the 180th hr in the no-forcing submesoscale generation experiment. The air temperature is set as such to provide a neutral initial condition. The constant relative humidity at a height of 2 m is 80%. Because strong accelerations can be introduced by wind forcing in the ocean surface layer, which can introduce numerical instability, the horizontal viscosity and diffusivity are set to  $0.1 \text{ m}^2 \text{ s}^{-1}$ , and the vertical viscosity and diffusivity are set to  $0.005 \text{ m}^2 \text{ s}^{-1}$ , per Thomas & Lee, 2005. Aside from the increased diffusivities and viscosities, all other parameters in the 24-hr ocean model forced by the uniform wind remain the same as those used in the 180-hr no-forcing model. The sudden increase in diffusivities/viscosities to allow for the wind forcing requires adjustment of the model. Thus, the contrast experiments are implemented after the 24-hr wind forcing run to ensure the model adjustment is complete.

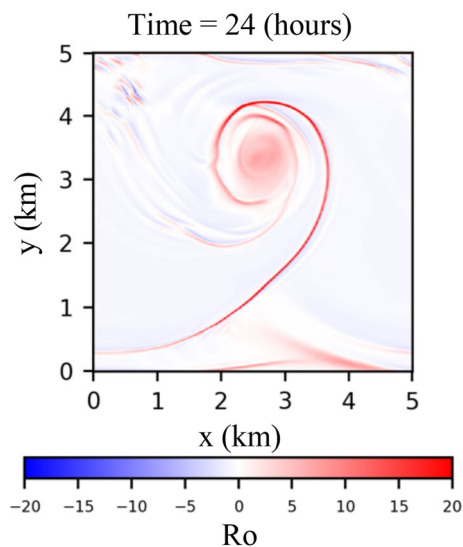


**Figure 3.** Surface Rossby Number forced by  $4 \text{ m s}^{-1}$  westward wind at 24 hr.

## 2.2. Contrast Experiments

The surface field of the local Rossby number (ratio of relative vorticity to planetary vorticity) after the 24-hr wind forcing submesoscale generation experiment is shown in Figure 3, in which a submesoscale eddy along with a strong front are evident. Using this ocean field as the initial condition and the atmospheric elements in the 24-hr wind forcing submesoscale generation experiment, two subsequent experiments (A and B) are conducted. In experiment A, the wind stress is calculated using Equation 1, the same as in the 24-hr wind forcing experiment. In experiment B, the surface current is absent in the wind stress calculation, as indicated in Equation 7:

$$\tau = \rho C_D \left( T_{\text{atm}, \text{SST}}, \bar{U} \right) \left( \bar{U} \right) |\bar{U}| \quad (7)$$

Both experiments (A and B) run for 6 hours.

Comparison between the initial wind stress fields calculated in experiments A and B are used to isolate the response of wind stress field to the submesoscale surface currents (Sections 3.1 and 3.2). Uniform fields of passive tracers with a concentration of  $0.01 \text{ m}^{-2}$  are released in the surface layer at the beginning of each experiment to investigate the influence of wind stress (with and without the inclusion of surface currents) on surface subductions and vertical transports associated with the submesoscale processes.

## 3. Results and Discussion

### 3.1. Wind Stress Response to Submesoscale SST Gradients

Wind stress adjustments to warm/cool water suggest that wind stress curl/divergence can be generated over a crosswind/downwind SST gradient (Maloney & Chelton, 2006). This has been revealed in satellite observations that show positive linear relationships between crosswind/downwind SST gradients and wind stress curl/divergence in meso- and largescale regimes (e.g., Chelton et al., 2004). In submesoscale studies, much stronger SST gradients have been reported from both observations and numerical simulations (D'Asaro et al., 2011; McWilliams, 2016; Stamper & Taylor, 2017), and yet their impact on wind stress curl/divergence are still quantitatively unclear. Here, using the submesoscale numerical results from this study, we quantitatively assessed the relationships between wind stress curl/divergence and crosswind/downwind SST gradients to determine whether SST gradients can significantly influence the wind stress field in the submesoscale regime.

Using the initial condition of the contrast experiments, wind stress curl fields are calculated according to Equation 7 (Figure 4a) and Equation 1 (Figure 4b), respectively. Comparing the front segment outlined in black with the eddy outlined in blue, we see the maximum magnitude of wind stress curl/divergence over the front segment is much greater than those over the eddy, suggesting that stronger crosswind SST gradients are over the front. The relationship between wind stress curl and crosswind SST gradients over the eddy/front segments is exhibited in Figures 6a and 6b/Figures 6c and 6d, respectively. To quantify the linear relationships, Pearson correlation coefficients ( $R$ ), which assume linearity (Benesty et al., 2009), were calculated for Figure 6 and following Figures 8, 9, 11 and 12. With surface currents excluded in wind stress (Equation 7), positive linear relationships between wind stress curl and crosswind SST gradients are revealed in Figure 6a (eddy) and Figure 6c (front), which are similar to those derived from satellite observations at meso- and large-scales (Chelton et al., 2004). Previous studies have raised two mechanisms to explain the impact of SST coupling on wind stress: (I) surface wind acceleration/deceleration attributed to the surface atmospheric pressure gradient across an SST gradient (Lindzen & Nigam, 1987; O'Neill et al., 2010; Small et al., 2008) and (II) wind stress modification due to the stabilization/destabilization of the atmospheric boundary layer over cool/warm waters (Hayes et al., 1989; Spall, 2007; Wallace et al., 1989). In order to determine its unique role that the wind stress modification (due to the stabilization/destabilization of the atmospheric boundary layer over cool/warm waters) plays, the atmospheric boundary layer is dynamically decoupled in the model to avoid mechanism (I). Thus, the wind adjustment to SST due to the pressure adjustment mechanism (Lindzen & Nigam, 1987; O'Neill et al., 2010; Small et al., 2008) is suppressed in this study primarily

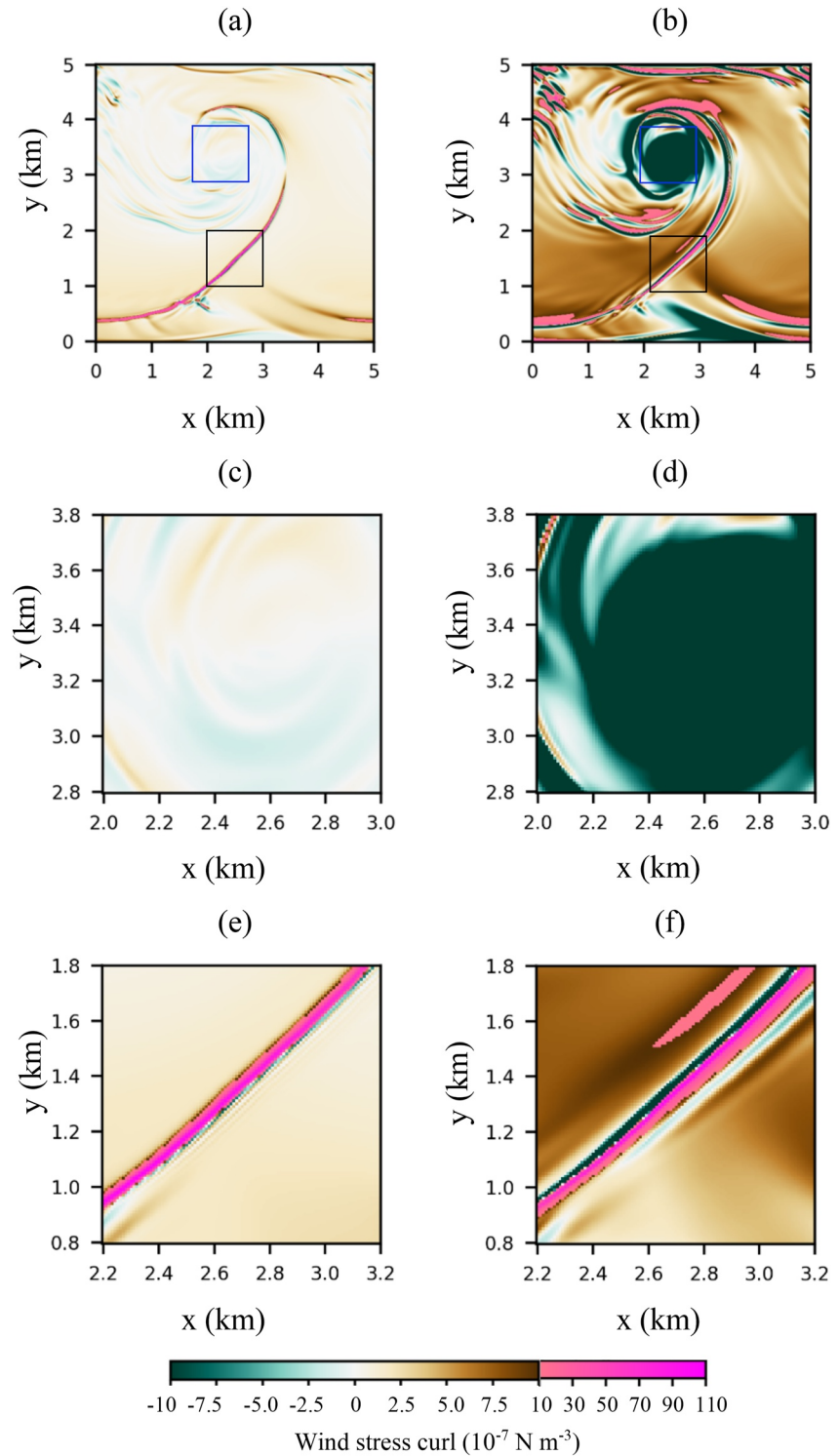


**Figure 4.** Wind stress curl calculated over the surface field in Figure 3. The calculation did not include surface currents in (a, c, e), but did in (b, d, f). The enlarged regions of eddy (blue boxes) and front segment (black boxes) are shown in (c, d) and (e, f) respectively.



because pressure gradients can cause substantial change to the wind on large scales (Lindzen & Nigam, 1987) and we focus on small scales.

The two-branch structure revealed in Figure 6c indicates that two different relationships between the wind stress curl and crosswind SST gradients exist over the front segment. It is diagnosed in Figure 7 to figure out the underlying mechanism. As indicated by red and blue dots in Figure 7a, two groups of wind stress curl fall within the same range of crosswind SST gradients. The blue dots (representing stronger wind stress curl) exhibited in Figure 7a are found on the cooler side of the front, whereas the red ones (representing weaker wind stress curl) can be seen in Figure 7b to be on the warmer side. Because the atmospheric temperature and 10 m wind speed are fixed and uniform, compared with the warmer side, the cooler side corresponds to a more stable stratification, which introduces weaker wind stress (Hayes et al., 1989; Spall, 2007; Wallace et al., 1989). Nonetheless, stronger wind stress curl is introduced by crosswind SST gradients on the cooler side, indicating the wind stress is more sensitive to SST over the cooler area where the stratification is more stable (see Figure 7c). This phenomenon is also consistent with the more sensitive response of the momentum transfer coefficient to the air-sea temperature difference in stable stratification with wind speeds of 4 m/s (Smith, 1988). The black dots in Figure 7a are found at the strongest SST gradients in Figure 7b, connecting the two branches on the two sides of the front.

Figure 5 shows the wind stress divergence fields with (Figures 5a, 5c and 5e) and without (Figures 5b, 5d and 5f) including surface current into the wind stress calculation. Similar to the relationship between wind stress curl and crosswind SST gradients, linear relationships between wind stress divergence and downwind SST gradients and the two-branch structure over the front are found in Figures 8a and 8c, where the surface currents are absent in the wind stress calculation. Nonetheless, the values of coupling coefficients defined by Maloney and Chelton (2006) as the slope of the linear relationships (ranging from 0.324 to 0.346) are smaller than those in satellite observations (0.57–1.88 in Chelton et al., 2004) and numerical results (0.5–0.89 in Shi & Bourassa, 2019). The small air-sea temperature differences (atmospheric temperature is prescribed as the average of SST), the lower wind speed than the averaged wind in open ocean ( $\sim 6.5 \text{ m s}^{-1}$ ), and the lack of surface wind acceleration/deceleration due to surface atmospheric pressure gradients across an SST gradient (O'Neill et al., 2010; Small et al., 2008) lead to the small coupling coefficients in our simulation.

### 3.2. Wind Stress Response to Submesoscale Surface Current Fields

The relative vorticity in the mesoscale usually much weaker than the planetary vorticity. Therefore, the effect of ocean surface current curl on the wind stress field has been ignored except in those regions with strong eddies and sharp fronts (Dewar & Flierl, 1987; Gaube et al., 2015). Nevertheless, the  $O(1)$  Rossby numbers (relative vorticities are in the same magnitude as the planetary vorticity) exhibited in the submesoscale regime has motivated interest in whether and how much the submesoscale relative vorticities/divergence can affect the wind stress curl/divergence.

Taking into account the positive surface current curl of the eddy in the wind stress calculation introduces corresponding negative wind stress curl, as shown in Figure 4d. In both Figures 6a and 8a, surface currents are absent in wind stress calculation. In Figures 6b and 8b, the surface currents are included in wind stress calculation, the wind stress curl/divergence over the submesoscale features a 20/10 times greater magnitude than those in Figures 6a and 8a, which signifies the dominant role of the surface currents in wind stress curl/divergence generation over the eddy. Moreover, the positive linear relationship between wind stress curl/divergence and crosswind/downwind SST gradients revealed in Figures 6a and 8a are no longer apparent when the surface current contribution is added (see Figures 6b and 8b).

On the other hand, over the submesoscale front magenta strips of robust wind stress curl are found in cases with (Figure 4f) and without (Figure 4e) surface current inclusion. The wind stress curl in Figure 6d, which encompasses the surface current contribution, still exhibits the same magnitude as the one in Figure 6c. However, if we focus on a specific range of SST gradients, such as where the crosswind SST gradients are greater than  $260^\circ\text{C}/100 \text{ km}$  in Figures 6c and 6d, the strong positive wind stress curl ( $80 \times 10^{-7}$  to  $100 \times 10^{-7} \text{ N m}^{-3}$ ) induced purely by crosswind SST gradients can be seen in Figure 6c. Whereas in Figure 6d, the wind stress curl becomes negative ( $0 \times 10^{-7}$  to  $-50 \times 10^{-7} \text{ N m}^{-3}$ ) with the inclusion of the surface currents. Comparing the maximum peak of wind stress curl in Figure 6c with the minimum point in Figure 6d, which contains surface currents in the wind stress calculation, we see a negative contribution of wind stress curl as robust as

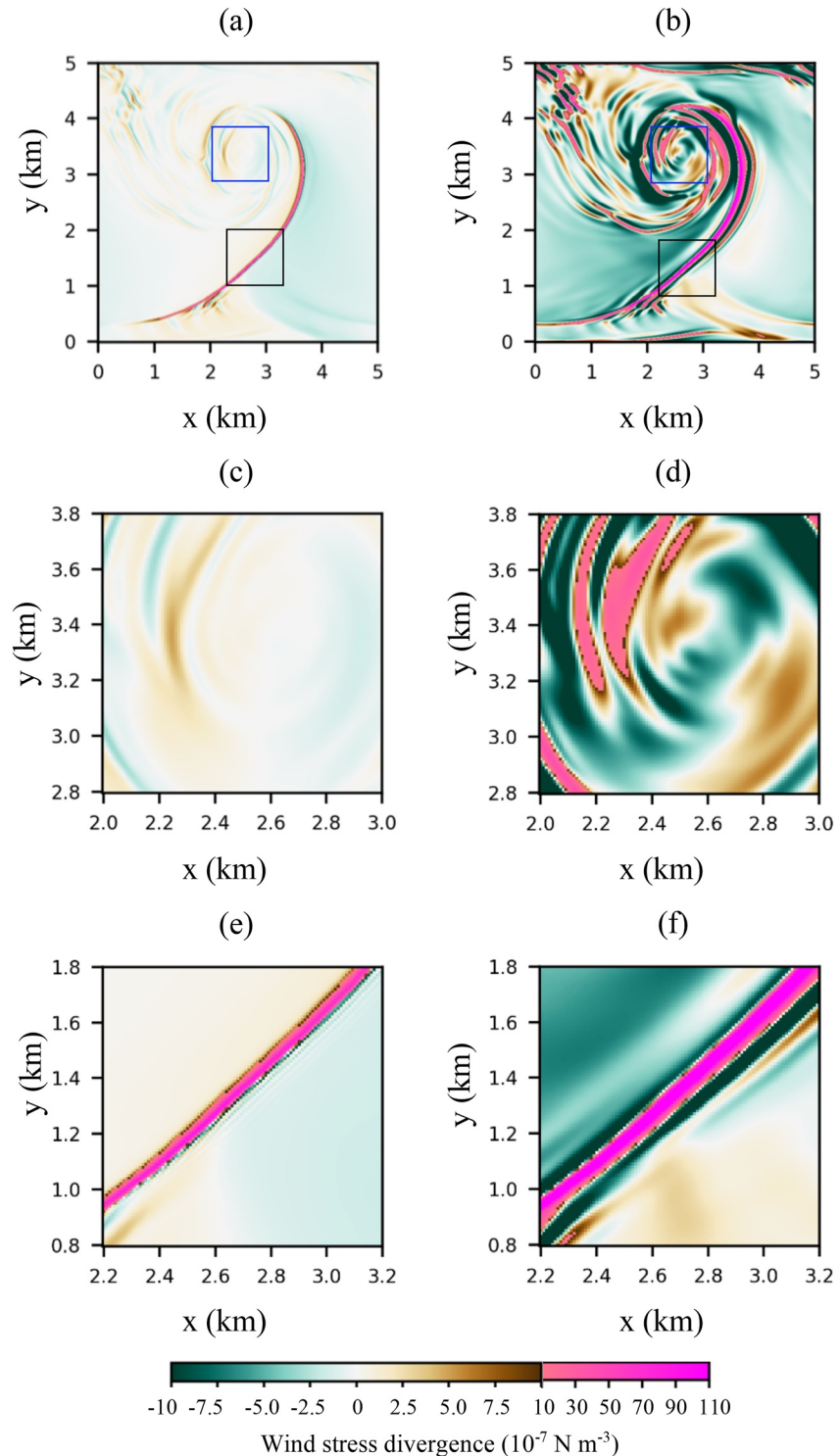


**Figure 5.** Same as Figure 4, except for wind stress divergence.

$-120 \times 10^{-7} \text{ N m}^{-3}$ . This is greater but of the same magnitude as the contribution due to the crosswind SST gradients ( $\sim 100 \times 10^{-7} \text{ N m}^{-3}$  in Figure 6c) over the front segment. Analogously, the wind stress divergence introduced by the surface current inclusion is of the same magnitude as the wind stress divergence due to the downwind SST gradients over the front segment, as shown in Figures 8c and 8d. For example, in the range where downwind SST gradients are greater than  $240^\circ\text{C}/100 \text{ km}$  in Figures 8c and 8d, the wind stress divergence only

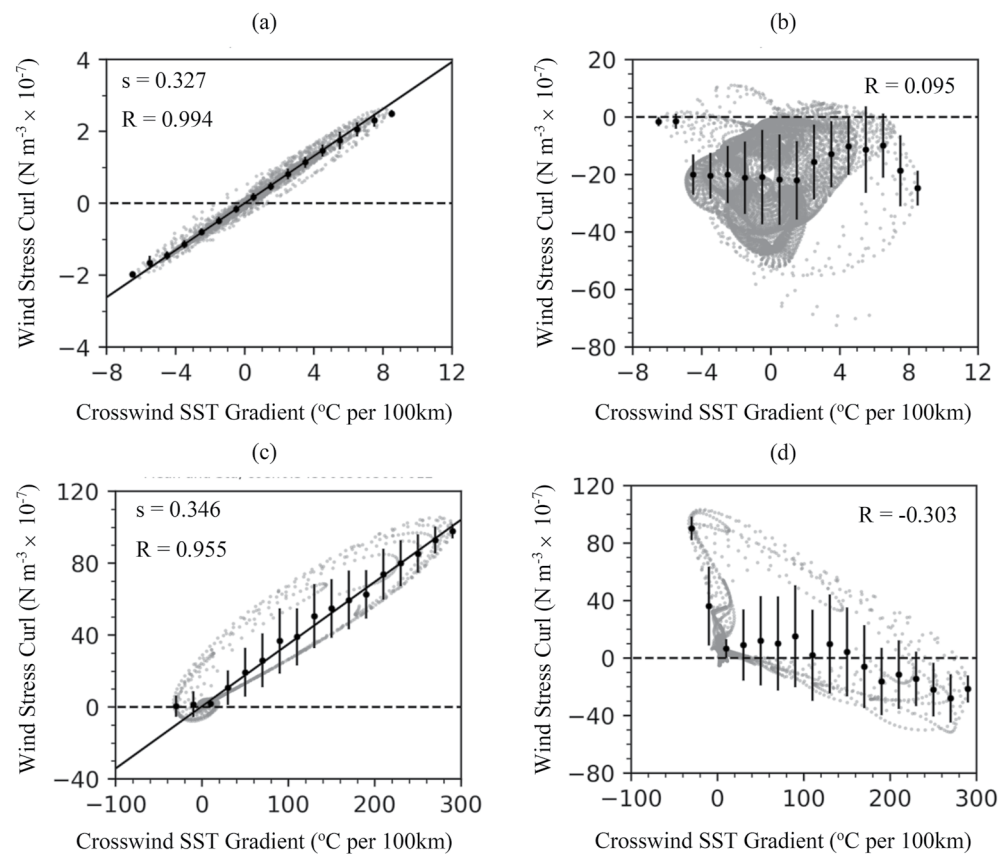


**Figure 6.** Wind stress curl as a function of crosswind sea surface temperature (SST) gradient for the submesoscale eddy (top panels) and front segment (bottom panels). The calculation did not consider surface currents in (a, c) but did in (b, d). Black dots and error bars are binned means and standard deviations. In (a) and (c), the slope values ( $s$ ) of least squares fitted black lines based on the binned averages represent the coupling coefficient between SST and surface wind stress. The Pearson correlation coefficients between crosswind SST gradients and wind stress curl are shown as the  $R$  values.

introduced by downwind SST gradients is around  $80 \times 10^{-7} \text{ N m}^{-3}$  in Figure 8c, but the wind stress divergence changes to around  $180 \times 10^{-7} \text{ N m}^{-3}$  when surface currents are included in Figure 8d. Thus, including surface currents in the wind stress calculation yields a wind stress divergence increment of  $100 \times 10^{-7} \text{ N m}^{-3}$  when the downwind SST gradient is greater than  $240^\circ\text{C}/100 \text{ km}$  in Figure 8d. The wind stress divergence increment introduced by the surface current ( $100 \times 10^{-7} \text{ N m}^{-3}$ ) is slightly greater but is still of the same magnitude as the wind stress divergence introduced by the downwind SST gradients ( $80 \times 10^{-7} \text{ N m}^{-3}$  in Figure 8c). In summary, because the SST gradients are of great magnitudes ( $>240^\circ\text{C}/100 \text{ km}$ ) over the submesoscale front segment, the wind stress curl/divergence introduced by SST gradients has the same magnitudes as the wind stress curl/divergence introduced by surface currents. When surface currents and SST gradients introduce wind stress curl of opposite signs, the contributions offset each other and leave a weak wind stress curl (Figure 6d). Likewise, they can compound each other to produce a strong wind stress divergence when of the same sign (Figure 8d).

When surface currents are taken into account for calculating wind stress, the relationship between wind stress curl/divergence and crosswind/downwind SST gradients is no longer a positive linear relationship (as shown in Figures 6b, 6d, 8b, and 8d), indicating that wind stress curl/divergence is not dominantly introduced by SST gradients over eddy and front segments. The negative linear associations between wind stress curl/divergence and current curl/divergence shown in Figure 9 demonstrate that surface current is the dominant force in introducing submesoscale wind stress curl/divergence. While it is smaller than the strength of the observed surface current vorticity up to  $100 f$  ( $f$  is the Coriolis frequency) in Raschle et al. (2020), the maximum value of surface current curl which is about  $34 f$  (Figure 9c) in this study implies that the influence of the surface current curl could be stronger in the ocean. Comparing to the observed strong surface current vorticity ( $\sim 100 f$ ) in Raschle et al. (2020), the smaller value of current gradients in the present study indicates that the model does not provide an overly

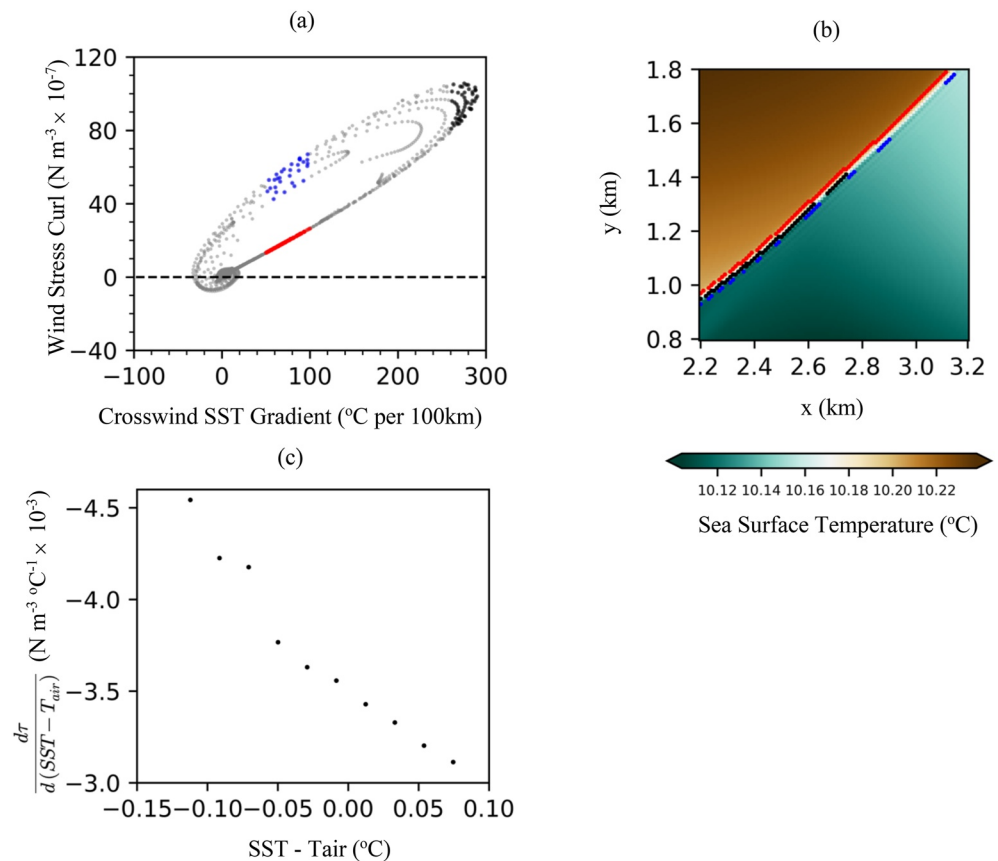


**Figure 7.** Same as in Figure 6 (c), gray dots in (a) are wind stress curl as a function of crosswind sea surface temperature (SST) gradient for the submesoscale front segment. The color shade in (b) is SST of the same region. The spatial locations of the red, blue, and black dots in (a) are shown in (b). (c) Shows the relation between the derivative of wind stress with respect to air-sea temperature difference and the air-sea temperature within the domain of (b).

exaggerated current field with extremely strong current gradients. Instead, the submesoscale dynamics in the model are simulated in a reasonable manner. Similar to what is shown in Figures 6c and 8c, the two-branch structures in Figure 9 manifest the influence of the distinct air-sea temperature differences over the two sides of the submesoscale front.

### 3.3. Wind Stress Response to Mesoscale Surface Features

With both SST gradients and surface currents taken into account, the relationship between wind stress curl/divergence and crosswind/downwind SST gradient in the 10 m resolution submesoscale numerical field have been found to be distinct from the relationship between wind stress curl/divergence and crosswind/downwind SST gradient in the 25 km resolution satellite observations (Chelton et al., 2004). However, the gap between the fine 10 m resolution scale and coarse 25 km resolution scale allowed space for an intermediate scale with dynamical importance—the mesoscale. To bridge the gap between the submesoscale and the satellite data, wind responses to mesoscale fields with a resolution of 5 km are investigated in this study.

As shown in Figure 10, a mesoscale eddy and a front segment in the Gulf of Mexico are designated in the black boxes, the model details for which can be found in Gopalakrishnan, Cornuelle, and Hoteit (2013), Gopalakrishnan, Cornuelle, Hoteit, Rudnick, and Owens (2013). As discussed, wind stress over these two domains is calculated using the same atmospheric properties which are used in the submesoscale domains, except that the air temperature is the mean value of the initial SST field of each mesoscale domain. The purpose of calculating wind stress over the mesoscale structures using the same method used for the submesoscale is to provide a comparison aimed at investigating the influence of scales on the air-sea coupling of SST and surface current. With surface currents

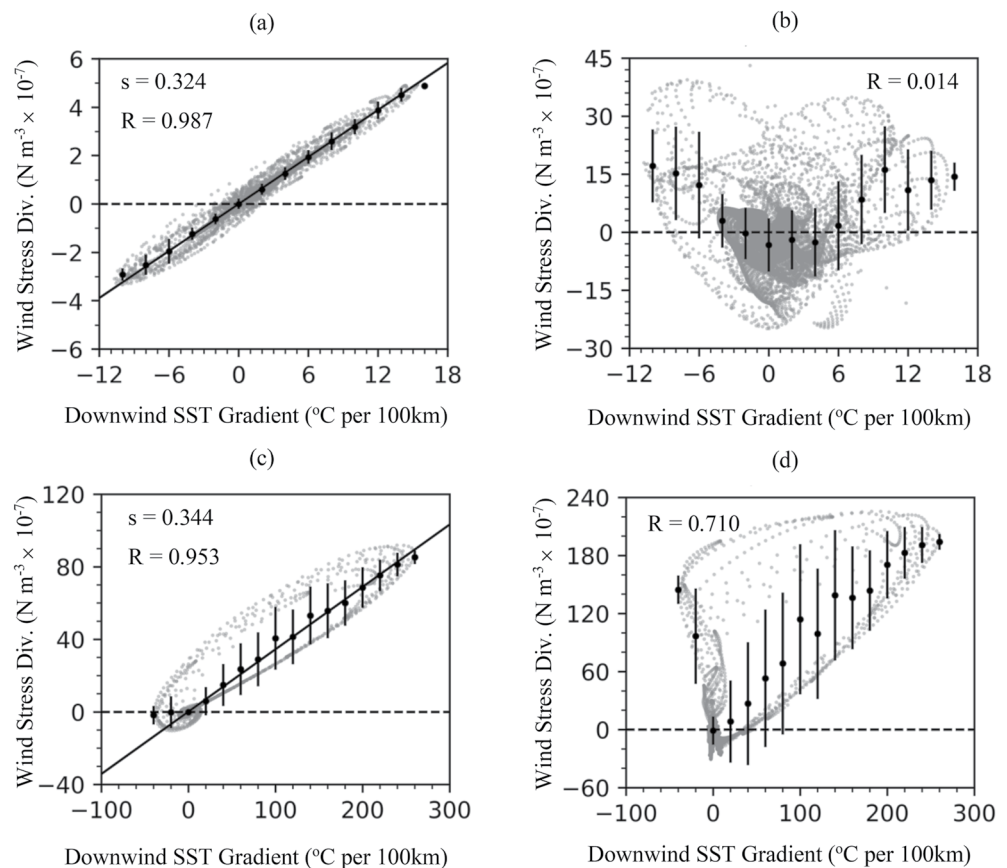


**Figure 8.** Wind stress divergence as a function of downwind sea surface temperature (SST) gradient for the zoom-in eddy (top panels) and front segment (bottom panels). The calculation did not consider surface currents in (a, c) but did in (b, d). Black dots and error bars are binned means and standard deviations. In (a) and (c), the slope values ( $s$ ) of the least squares fitted black lines based on the binned averages represent the coupling coefficient between SST and surface wind stress. The Pearson correlation coefficients between downwind SST gradients and wind stress divergence are shown as the  $R$  values.

absent in the wind stress calculation, the wind stress curl in Figure 11a presents a clear positive linear dependence on crosswind SST gradients over the mesoscale eddy ( $R = 0.979$ ). Similarly, a positive linear trend was found over the front ( $R = 0.858$  in Figure 11c) with a two-branch structure caused by the distinct air-sea temperature difference on both sides of the front. The inclusion of surface currents has made the dots representing wind stress curl more dispersive in Figure 11b ( $R = 0.418$ ) and Figure 11d ( $R = 0.838$ ), suggesting the wind stress curl induced by surface currents has disturbed its linear dependence on the SST gradients. Still, differentiating from the complete irregularities over the submesoscale eddy and front depicted in Figures 6b, 6d, 8b, and 8d ( $R$  are 0.095,  $-0.303$ , 0.014, and 0.719 respectively), weak positive correlations still exist between the mesoscale wind stress curl and crosswind SST gradients ( $R$  is 0.418 in Figure 11b and 0.838 in Figure 11d), which is an indication of stronger associations between wind stress curl/divergence and SST gradients (stronger air-sea coupling with SST) in the mesoscale than in the submesoscale.

In Figure 11c, the bottom branch with a stronger negative wind stress curl is also found on the cooler side of the front (not shown in this paper), suggesting that a more stable stratification over the cooler side where the wind stress is more sensitive to temperature (comparing to the warmer side) when the wind speed is  $4 \text{ m s}^{-1}$ . Despite the same magnitudes of crosswind SST gradients over the mesoscale eddy and front (Figures 11a and 11c), the strongest negative wind stress curl over the cooler side of the front (Figure 11c) is about four times greater than that seen over the eddy (Figure 11a). Both the two-branch structures found in the mesoscale and submesoscale domains when not considering surface currents indicate that not only is wind stress curl a linear function of crosswind SST gradient, but the slope (coupling coefficient) of the linear function is also

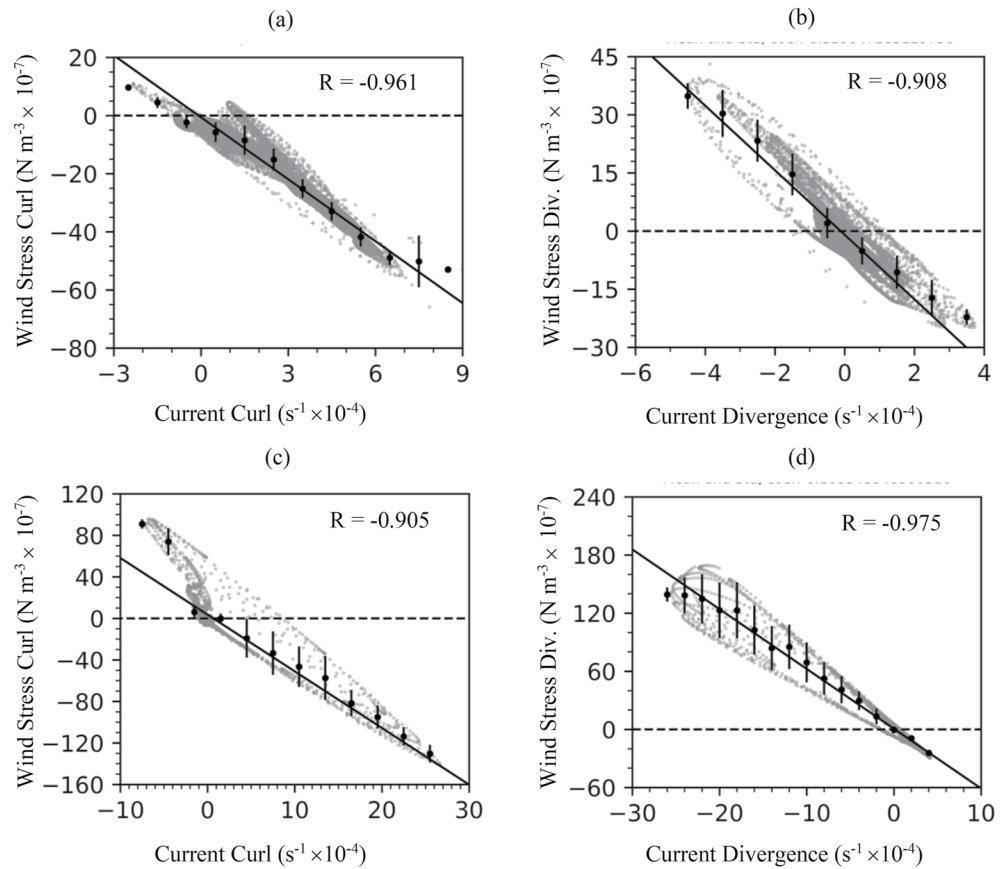


**Figure 9.** Wind stress curl (a, c)/divergence (b, d) as a function of current curl/divergence for the submesoscale eddy (top panels) and front segment (bottom panels). Black dots and error bars are binned means and standard deviations. The black lines are least squares fitted lines based on the binned averages. The Pearson correlation coefficients between current curl/divergence and wind stress curl/divergence are shown as the  $R$  values.

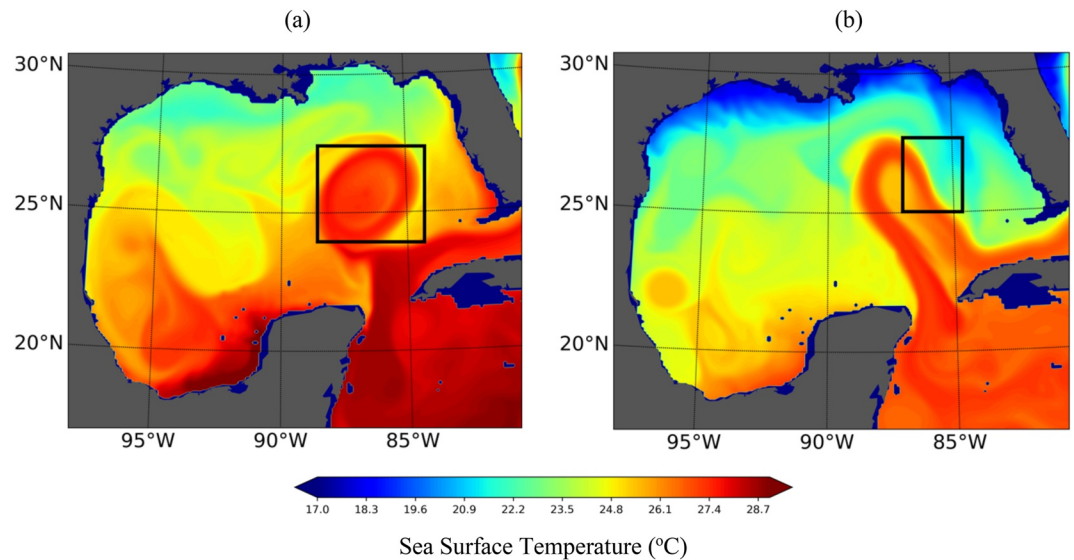


**Figure 10.** Sea surface temperature of Gulf of Mexico at 7 May 2013 (a) and 31 January 2012 (b). An eddy region and a front segment region are shown by the black boxes in (a) and (b), respectively.

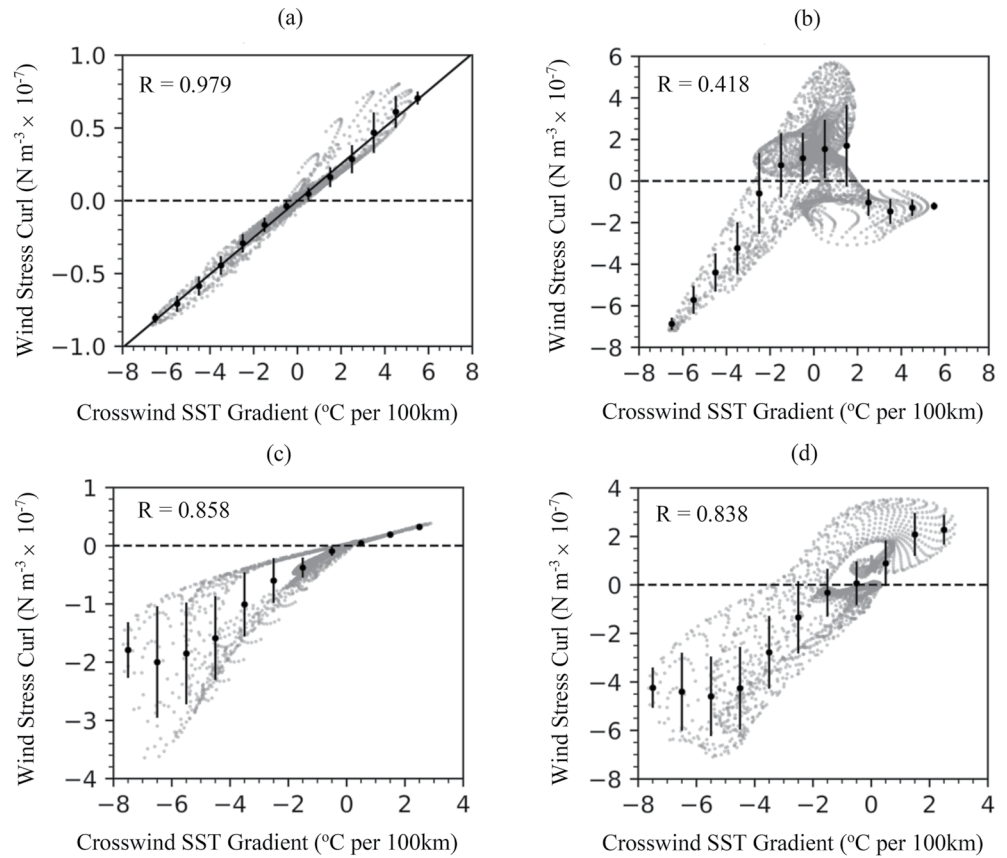


**Figure 11.** Wind stress curl as a function of crosswind sea surface temperature (SST) gradient for the mesoscale eddy (top panels) and front segment (bottom panels). The calculation did not consider surface current in (a, c) but did in (b, d). Black dots and error bars are binned means and standard deviations. In (a) and (c), the positive slopes of least squares fitted black lines based on the binned averages represent the coupling between SST and surface wind stress. The Pearson correlation coefficients between crosswind SST gradients and wind stress curl are shown as the  $R$  values.

dependent on the air-sea temperature difference (stratification). In contrast to the submesoscale front segment, the mesoscale front has weaker SST gradients but greater temperature differences across the front, resulting in the more dispersive (wider) tail of wind stress curl that falls in the strong negative crosswind SST gradients as shown in Figure 11c.

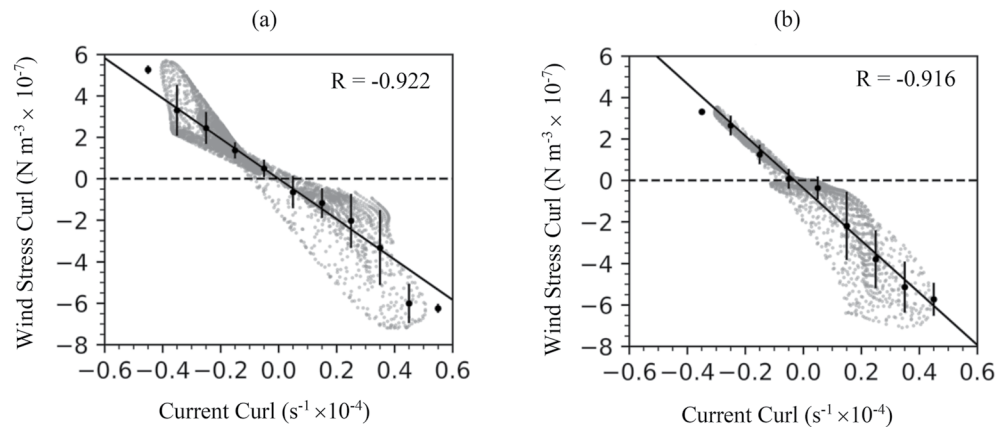


**Figure 12.** Wind stress curl as a function of current curl for the mesoscale eddy region (a) and front segment region (b). Black dots and error bars are binned means and standard deviations. The black lines are least squares fitted lines based on the binned averages. The Pearson correlation coefficients between current curl and wind stress curl are shown as the  $R$  values.

With surface currents taken into account in the wind stress calculation, the strongest wind stress curl is increased from  $\pm 1 \times 10^{-7} \text{ N m}^{-3}$  (Figure 11a) to  $\pm 7 \times 10^{-7} \text{ N m}^{-3}$  (Figure 11b) over the mesoscale eddy, and is enhanced from  $-4 \times 10^{-7} \text{ N m}^{-3}$  (Figure 11c) to  $-7 \times 10^{-7} \text{ N m}^{-3}$  (Figure 11d) over the mesoscale front. Furthermore, the relationship between crosswind SST gradients and wind stress curl over the mesoscale eddy ( $R = 0.418$  in Figure 11b) and front segment ( $R = 0.838$  in Figure 11d) are no longer strictly positive linear. However, compared with the weak and negative correlations between the wind stress curl and crosswind SST gradients in the submesoscale eddy ( $R = 0.095$  in Figure 6b) and front ( $R = -0.303$  in Figure 6d), the mesoscale eddy and front still exhibit positive correlations between wind stress curl and crosswind SST gradients that are more similar to the positive linear relationships in satellite observations (e.g., Chelton et al., 2004).

The dependence of wind stress curl on surface current curl over the mesoscale eddy and front segment is depicted in Figure 12, indicating the wind stress curl is negatively correlated to surface current curl. Because intense current curl is usually associated with strong SST gradients in the mesoscale regime, these SST gradients can introduce wind stress curl and lead to a significant variance in the linear relationship between wind stress curl and surface current curl, as shown in Figure 12. Comparing the wind stress curl over the mesoscale eddy (Figure 12a) and submesoscale eddy (Figure 9a) when surface currents are included in the wind stress calculation, the magnitude of wind stress curl introduced over the submesoscale eddy ( $60 \times 10^{-4} \text{ s}^{-1}$  in Figure 9a) is about 10 times greater than that over the mesoscale eddy ( $6 \times 10^{-4} \text{ s}^{-1}$  in Figure 12a). Whereas the crosswind SST gradients over the mesoscale eddy ( $0.06^\circ\text{C km}^{-1}$  in Figure 11a) and the submesoscale eddy ( $0.08^\circ\text{C km}^{-1}$  in Figure 6a) have the same magnitude. Thus, the significant difference in wind stress curl between the mesoscale eddy and the submesoscale eddy is mainly due to their distinction in magnitudes of current curl ( $7 \times 10^{-4} \text{ s}^{-1}$  for the submesoscale eddy shown in Figure 9a and  $0.5 \times 10^{-4} \text{ s}^{-1}$  for the mesoscale eddy in Figure 12a). On the other hand, the magnitude of crosswind SST gradients over the submesoscale front ( $3^\circ\text{C km}^{-1}$  in Figure 6c) being more than 30 times greater than those over the mesoscale front ( $0.08^\circ\text{C km}^{-1}$  in Figure 11c), along with the surface current curl over the submesoscale front ( $25 \times 10^{-4} \text{ s}^{-1}$  in Figure 9c) being about 50 times greater than that over the mesoscale front ( $0.5 \times 10^{-4} \text{ s}^{-1}$  in Figure 12b), much stronger wind stress curl is introduced over the submesoscale front ( $140 \times 10^{-7} \text{ N m}^{-3}$  in Figure 9c) than over the mesoscale front ( $7 \times 10^{-7} \text{ N m}^{-3}$  in Figure 12b).

The comparison between the 5 km resolution mesoscale fields and the 10 m resolution submesoscale fields confirms that the much finer and sharper SST gradients and surface current vorticity resolved in the high-resolution model can introduce an even stronger wind stress curl. Specifically, the inclusion of surface currents can introduce significantly strong wind stress curl over the submesoscale eddy and the front. In the next section, the influence of the enhanced submesoscale wind stress curl due to the inclusion of surface currents on vertical transports and PV distribution in the ocean is investigated.

### 3.4. Oceanic Vertical Transports Response to Wind Stress Fields

The oceanic submesoscale processes are characterized by strong convergence zones and vertical velocities (Balwada et al., 2018; D'Asaro et al., 2018; Thomas et al., 2008) that trap floating materials and transport them vertically. The vertical transports are of special interest because local upwelling and downwelling can impact the availability of nutrients (Lévy, Lovino, et al., 2012; Lévy et al., 2018; Mahadevan, 2016; McGillicuddy et al., 2003) and  $\text{CO}_2$  (Köhn et al., 2017; Sabine & Tanhua, 2010). To examine the influence of the submesoscale-modified wind stress fields on these convergence zones and the associated vertical transports, two identical uniform tracer fields were added to the surface layer of the two contrasting experiments as initial conditions because the evolution of the passive tracer field can help visualize the processes of convergence and vertical transports. In addition, the experiment setups for Exp. A and Exp. B are identical except for the distinction in air-sea turbulent flux schemes (Equation 1 for Exp. A and Equation 7 for Exp. B). Thus, any difference in dynamics visualized by the tracer field comparison can be attributed to the inclusion/exclusion of surface currents in the air-sea turbulent flux scheme.

In order to obtain a horizontal view of distribution, the tracer concentration in Exp. A in the first 25 min is vertically averaged from surface to bottom as shown in Figure 13 with a 5-min interval. The initial averaged tracer concentration of  $1 \times 10^{-4} \text{ m}^{-3}$  is depicted in Figure 13a. A narrow strip with the higher tracer concentration along the submesoscale front appears 5 min later in Figure 13b. At the 10th min, the strength of the along-front convergence strip is enhanced, with some circular bands of weak divergence appearing at the edge of the eddy and a weak convergence zone at the center of the eddy. In Figures 13d–13f, the along-front convergence strip is



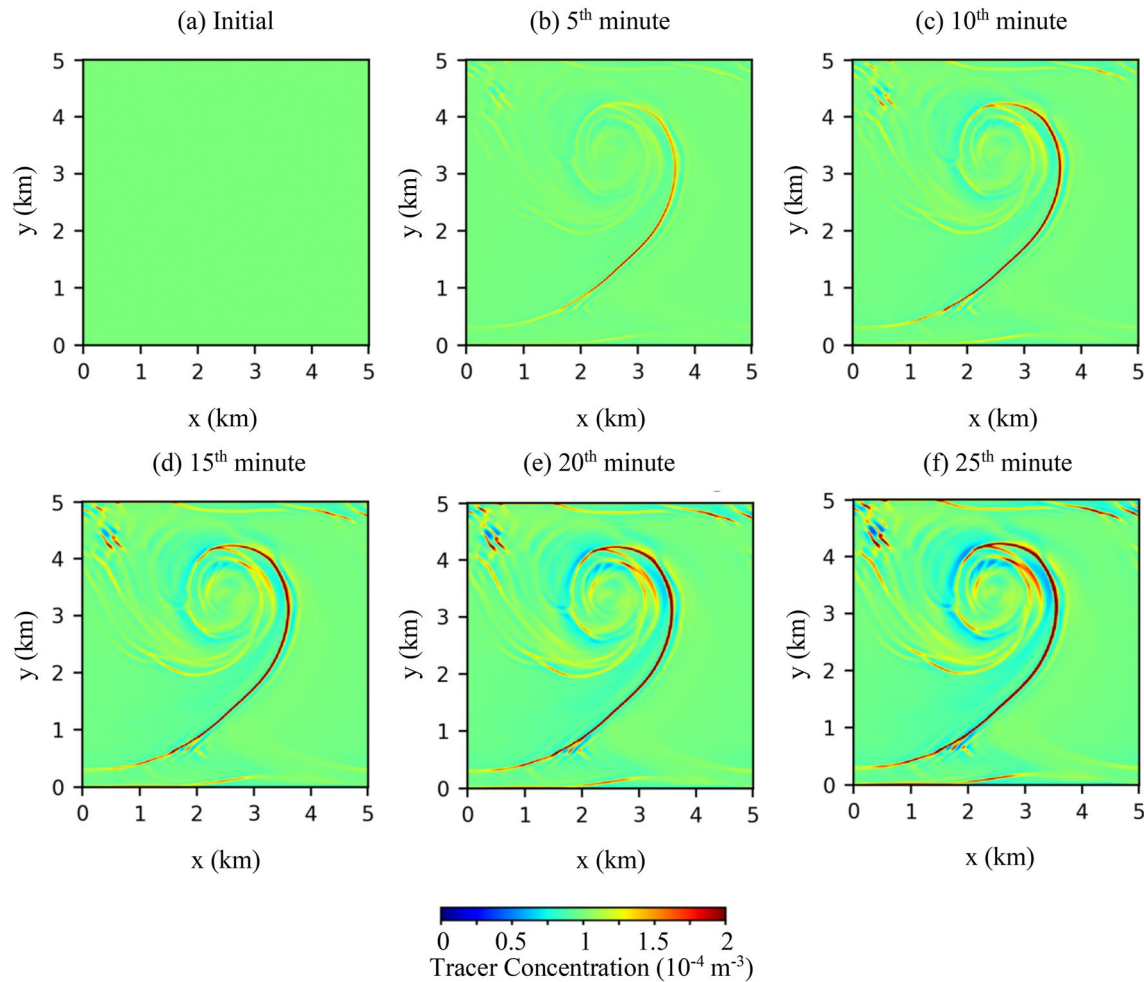


**Figure 13.** Vertically averaged tracer concentration from the surface to the bottom (100-m depth) within the first 25 min. The results of Exp. A are shown here, in which surface current is considered in the wind stress calculation.

further enhanced with time and extended around the eddy's edge. In addition, a few strong divergent and convergent bands form and grow within the eddy field. The dark red high-concentration tracer bands in Figure 13 reveal strong convergence structures along the front and around the eddy, suggesting the uniform initial tracer is transported and congregates along the submesoscale fronts and filaments.

Averaged throughout the entire depth (surface to 100 m depth) to exhibit the horizontal transport/distribution in Figure 13, the tracer concentration is also averaged from 50 m depth to 100 m depth to signify the vertical transport in Figure 14. Up to the 25th min, no noticeable tracer concentration is observed beneath the 50 m depth as Figure 14a shows. Nonetheless, 5 min later, the purple band appears in Figure 14b indicating a certain amount of tracer has been transported downward from the layers above the 50 m depth. This nonzero tracer band's length and strength continues to grow, as illustrated in Figures 14c–14f. At the 60th min in Figure 14f, the shape of the nonzero tracer band spatially matches up with the submesoscale front, indicating the passive tracer not only congregates along the submesoscale front but also is vertically transported into deeper layers through the front.

Compared to the horizontal distribution of tracer in Exp. A shown in Figures 13 and 14, Exp. B reveals similar patterns not shown here. Instead, the differences of the horizontally averaged tracer concentration between Exp. A and Exp. B (Exp. A minus Exp. B) are shown in Figure 15. The differences are horizontally averaged along  $x$  direction and only the portion between 2 and 3 km in the  $y$  axis are shown in the figure to avoid boundary complexities. The red band in Figure 15a, which represents a higher tracer concentration beneath the 50-m depth in Exp. A, strengthens over time as shown in Figures 15b–15f, suggesting more tracer is transported to deep layers with surface currents considered in the wind stress calculation. Two blue bands are also observed, of which

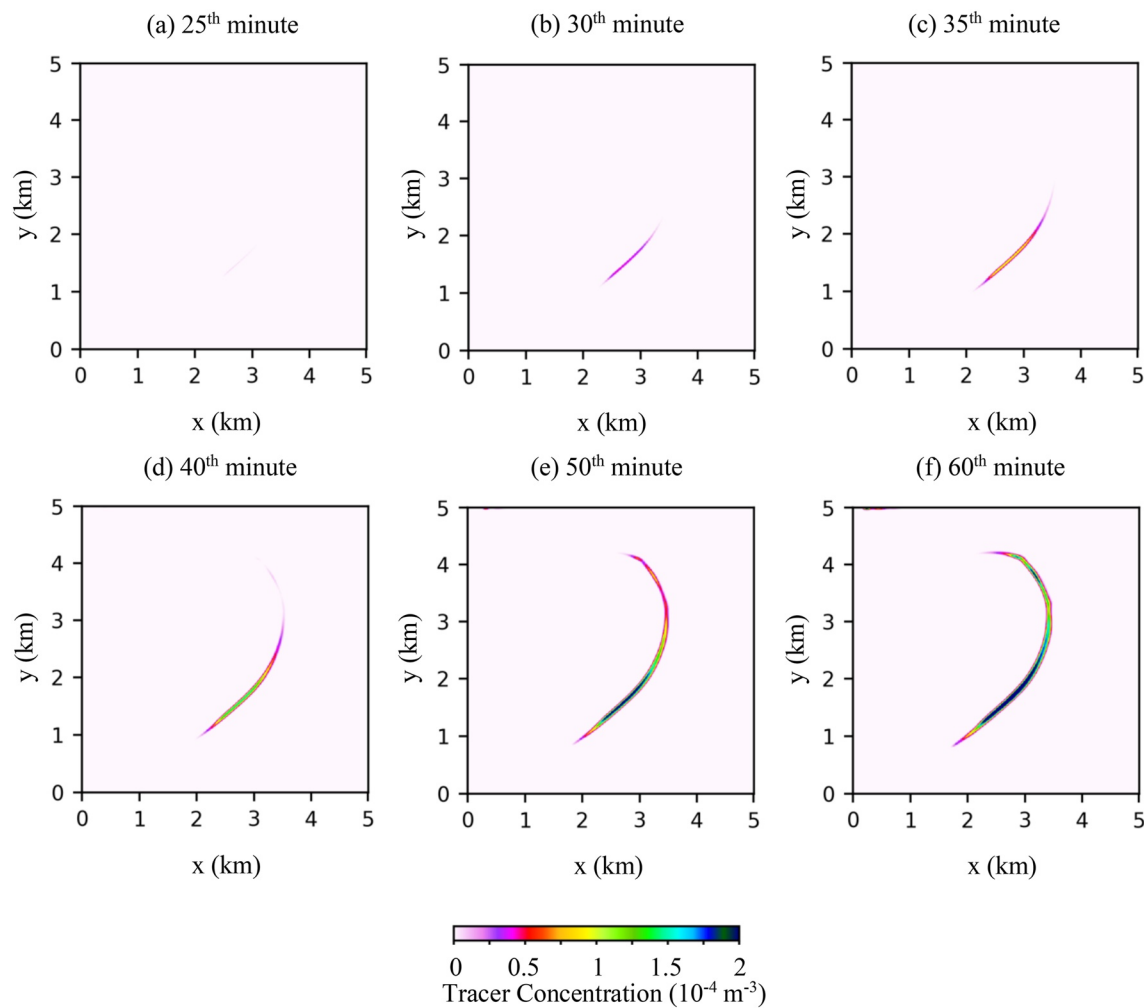


**Figure 14.** Vertically averaged tracer concentration from 50-m depth to bottom (100-m depth) between the 25th min and the 1st hr. The results of Exp. A are shown here, in which surface current is considered in the wind stress calculation.

one is beneath the surface, and the other one is above the red band. They manifest separately in Figure 15b and eventually merge together in Figure 15f. The blue band adjacent (above) the red band is an indication of stronger downward transports near surface and 50 m depth in Exp. A whereas the blue band near (beneath) the surface reveals Exp. A has a weaker subduction from the surface than Exp. B.

The vertical distributions of tracer in Exp. A and Exp. B are also quantitatively compared through the vertical profiles of horizontally cumulated tracer amount in Figure 16a. Because most of the tracer stays in the near surface layers and merely a small portion of it can be transported downward into deep layers, only the depth of 30–100 m is shown in Figure 16a to better detect the difference between Exp. A and Exp. B. The tracer amount beneath the 30 m depth increased from blue (2nd hr) to green (4th hr) and then to red (6th hr), providing evidence that the tracer has been transported downward from the upper layers in both experiments. The tracer amounts in Exp. A represented by the solid lines are less than those in Exp. B (dashed line) between the 30 and 50 m depth, and greater than Exp. B below the 50 m depth, revealing stronger vertical transports around 50 m depth in Exp. A. According to Table 1, Exp. A transports 10% more tracer beneath the 50 m depth than Exp. B in the first 5 hours. Overall, although Exp. A and Exp. B have identical initialization and surface wind, considering surface currents in the wind stress calculation in Exp. A introduces a stronger vertical transport around the 50-m depth. The probability density functions (PDF) of vertical velocity in Exp. A and Exp. B are shown in Figures 16b–16d. Because most of the vertical velocities in the domain grids are very small (close to zero), the PDF diagnosis is only shown for the spectrum of strong downward vertical velocities. The PDF comparisons in Figures 16b–16d

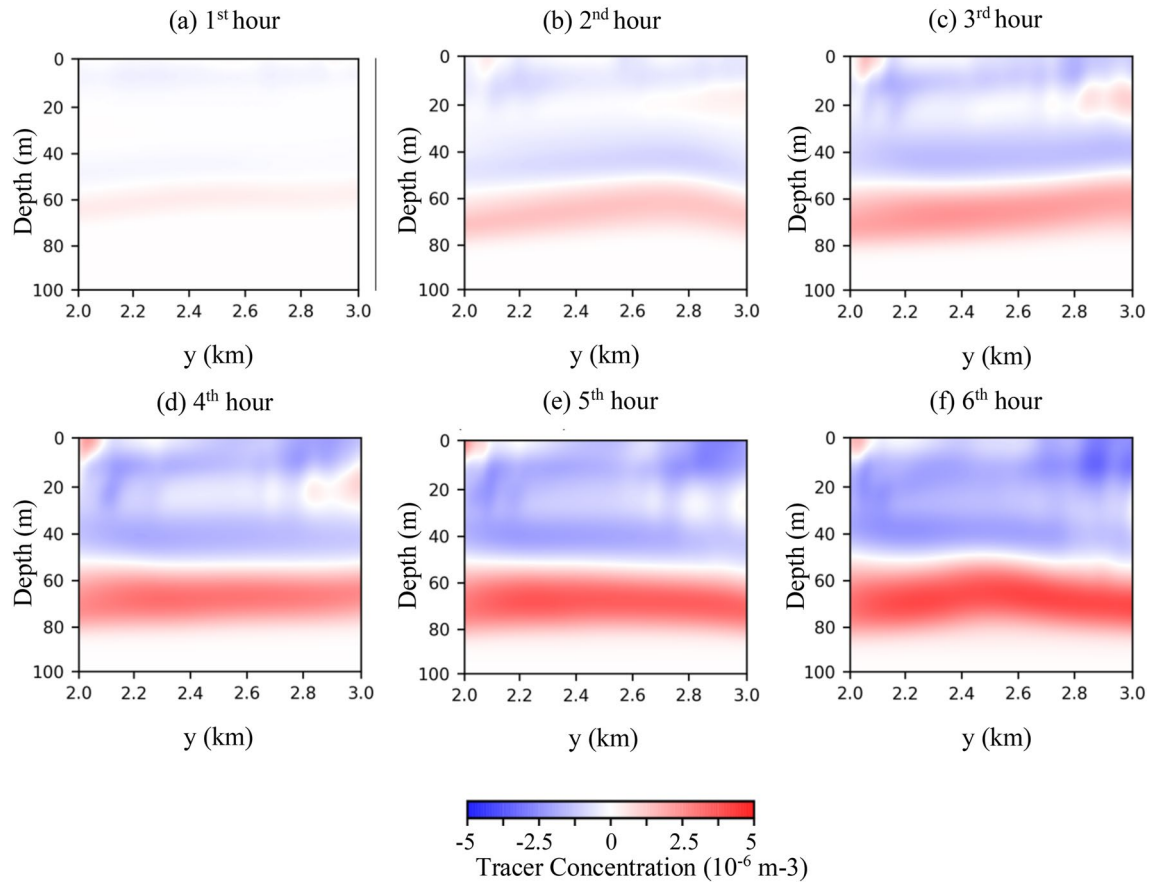


**Figure 15.** Horizontally averaged tracer concentration difference (Exp. A minus Exp. B) along the  $x$  direction. Only the results between the 2nd km and the 3rd km in the  $y$  direction are shown here.

reveal that the downward vertical velocities in depth between 40 and 60 m at 2nd, 4th, and 6th hr are also stronger in Exp. A (compared to Exp. B), which results in more of the passive tracer being transported from the surface to the interior. To further explore the dynamical impact of this phenomenon, PV fields of the two experiments are diagnosed next.

### 3.5. Implications for Potential Vorticity (PV) Distribution

Surface PV injection is an important air-sea interaction process. When the wind blows in the same direction as the surface currents, negative PV injection from the surface can induce front intensification (Mahadevan et al., 2008; Thomas & Lee, 2005) and stimulate instabilities (D'Asaro et al., 2011; Hoskins, 1974; Zhou et al., 2022). In this study's contrast experiments, negative PV is injected into the ocean because both the surface currents and wind are westward. As discussed above, the passive tracer initially at the surface horizontally converges along the submesoscale front and is vertically transported into deeper layers. Transported by water flow, PV can also be considered a passive tracer. Thus, the negative PV injected by current-direction wind forcing through the surface is expected to have the same pattern of motion as the passive tracer in the contrast experiment. The Hovmöller plot of horizontally averaged PV in the 24-hr wind forcing submesoscale generation experiment is shown in Figure 17. The PV is calculated according to Equation 8 (Marshall & Nurser, 1992):

$$PV = -\frac{1}{\rho} (f + \nabla \times \bar{u}) \cdot \nabla \sigma \quad (8)$$

where  $\rho$  is in situ density,  $f$  is Coriolis parameter,  $\bar{u}$  is velocity, and  $\sigma$  is potential density.

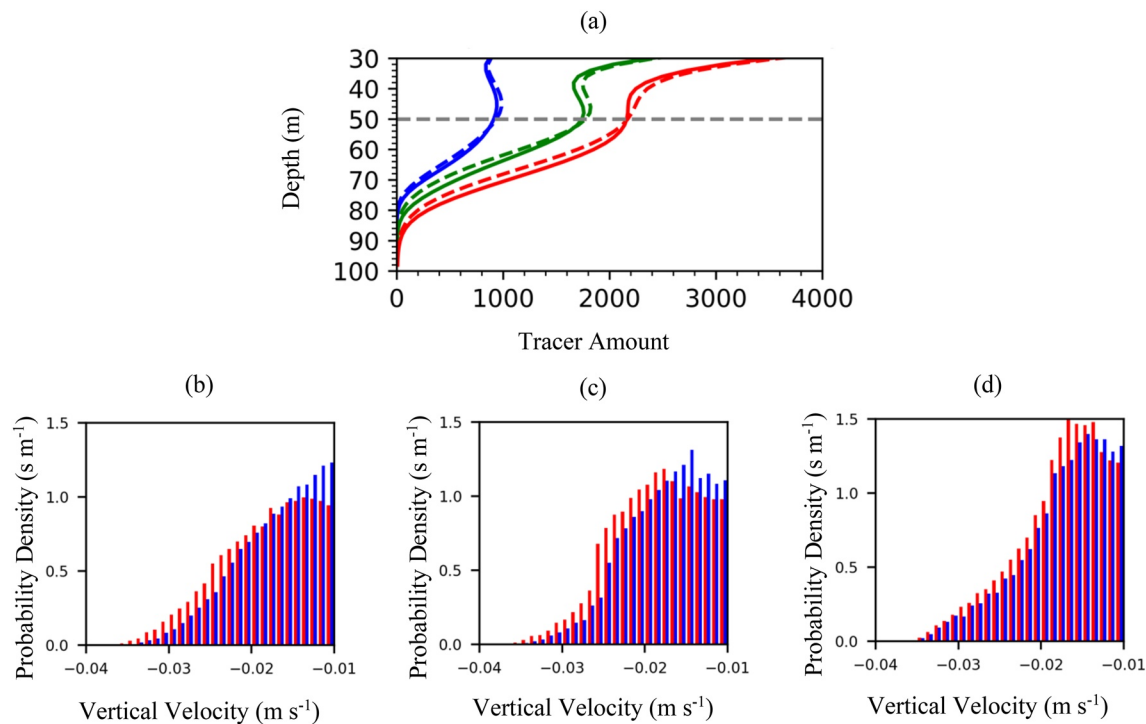


**Figure 16.** (a): vertical profiles of tracer which is horizontally integrated over both horizontal directions. The blue, green, and red lines represent profiles at 2nd, 4th, and 6th hr, respectively. Solid lines are for Exp. A and dashed lines are for Exp. B. Probability density function of downward vertical velocity stronger than  $1 \text{ cm s}^{-1}$  at depths between 40 and 60 m for Exp. A (red) and Exp. B (blue) at 2nd, 4th, and 6th hr are shown in (b), (c) and (d), respectively.

Being red over the entire column, the initial condition shows all the layers are of positive PV. However, when forced by wind for 1 hour, a few layers close to the surface turn blue, suggesting negative PV is being injected into the ocean through the surface and staying in the upper layers. This process continues such that the negative PV accumulating near the surface layers is eventually transported into deeper layers where it neutralizes the positive PV, as indicated by the attenuation of red coloring in the deep layers over time.

Similar to Figure 15, the difference in horizontally averaged PV concentration in the 6-hr tracer experiments (Exp. A minus Exp. B) is shown in Figure 18. Only the portion between 2 and 3 km in the y axis is exhibited to avoid boundary complexities. A deep red band near the surface is depicted in Figure 18a, indicating less negative (more positive) PV injected into the water in Exp. A. This phenomenon can be explained by the inclusion of surface currents in the Exp. A, which made the relative wind speed (between the same-direction surface wind and ocean surface) weaker than the absolute wind speed. Continuing the process of less negative PV being injected from the surface in Exp. A causes the near-surface red band to grow over time.

**Table 1**  
Comparison of the Amount of Tracer That Has Been Transported Beneath 50-M Depth in Exp. A and Exp. B

Time (hr)	Current (Exp. A)	No current (Exp. B)	Cur–No cur (Exp. A–Exp. B)	Percentage increase
1	4,087	3,991	96	2.4
2	8,411	7,919	492	6.2
3	12,088	11,062	1,026	9.3
4	16,592	15,125	1,467	9.7
5	20,841	18,932	1,909	10.1
6	24,741	22,402	2,339	10.4

An interesting phenomenon in Figure 18 is the parallel blue and red bands, which are beneath and beyond the 60 m depth, respectively. Both of the bands start to emerge around the 2nd hr (Figure 18b) and become more evident as time goes by (Figures 18c–18f). Blue/red represent more/less negative PV in Exp. A, and we see more negative PV is vertically transported through the 60 m depth in Exp. A. In contrast to the passive tracer, negative PV is dynamically active and can be neutralized by surrounding positive PV thus inducing instabilities. Therefore, the parallel bands indicating the PV difference in Figure 18 are not as clear and homogeneous as the bands representing the passive tracer difference in Figure 15.

Overall, the PV diagnosis in this study reveals a counterintuitive phenomenon: even when less negative PV is injected from the surface because surface currents are considered in the wind stress calculation, more negative PV is

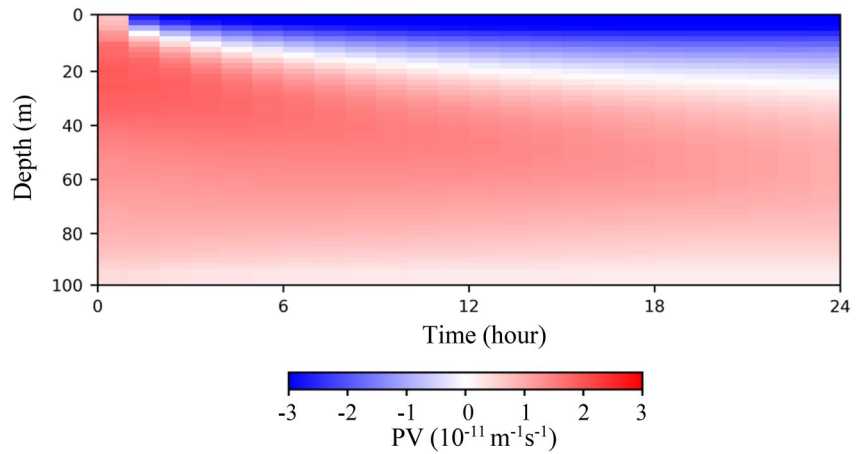


**Figure 17.** Hovmöller plot of horizontally averaged potential vorticity in the 24-hr wind forcing experiment.

vertically transported into deeper layers. Being capable of triggering instabilities and mixings in the surroundings with the opposite-sign PV, the negative PV transported into deeper layers has the potential to change the dynamics of the mixed layer, a process worthy of further investigation.

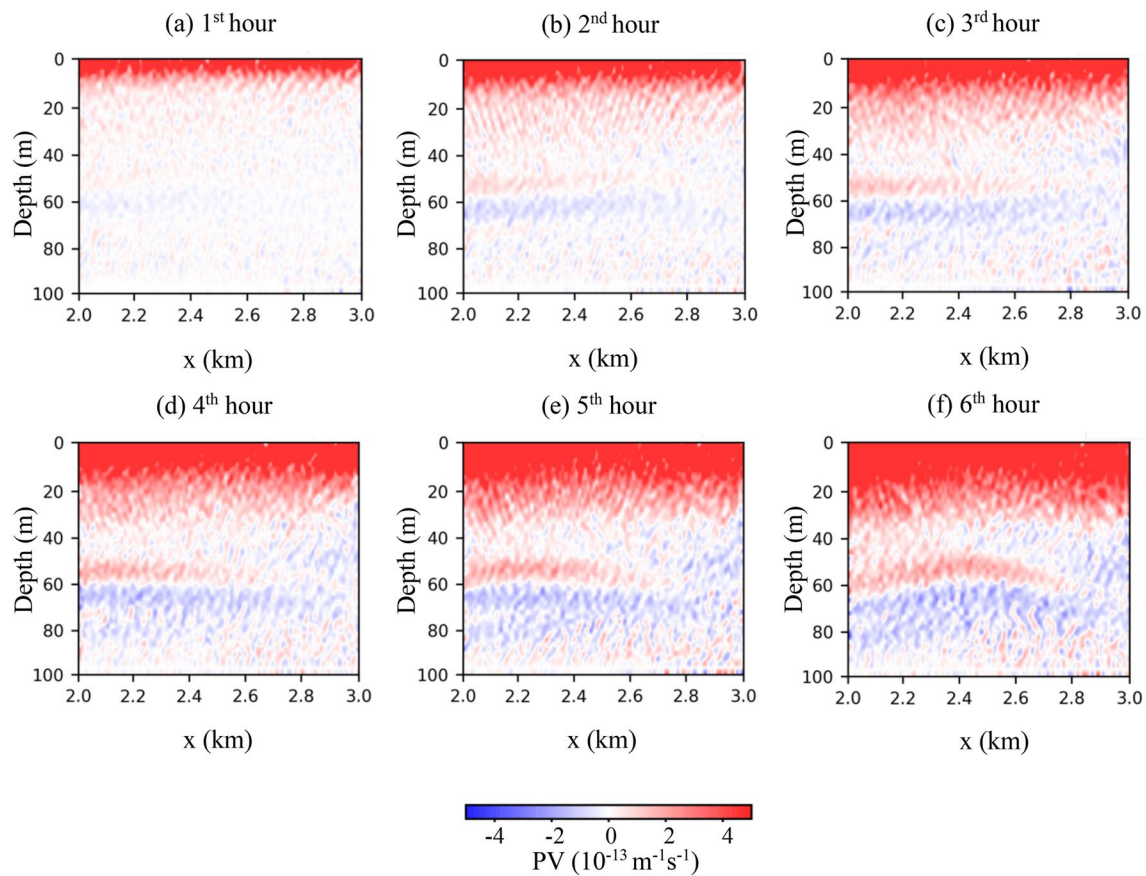


**Figure 18.** Horizontally averaged potential vorticity difference (Exp. A minus Exp. B) along the  $x$  direction. Only the results between the 2nd km and the 3rd km in the  $y$  direction are shown here. The surface current is considered in the wind stress calculation in Exp. A, but not in Exp. B.

#### 4. Conclusions

This numerical modeling study is designed to advance our understanding of the roles that SST gradients and surface currents play in the submesoscale air-sea interactions. This research was motivated by the richness of the submesoscale processes in the ocean revealed by high-resolution numerical models and observations and the importance of air-sea interaction in ocean-atmosphere coupled systems. It is argued that the wind stress field can be significantly influenced by submesoscale structures at the ocean surface. In addition, the submesoscale-modified wind stress can interact with the ocean surface to impact the submesoscale dynamics, passive tracer subduction, and PV distribution in the upper ocean.

The positive linear relationships between wind stress curl/divergence and crosswind/downwind SST gradients valid in mesoscale regime are examined over the ocean fields of a submesoscale front and an eddy. These linear relationships are found to remain valid in the submesoscale only when surface currents are absent in the wind stress calculations. When surface currents are included in the calculations, the relationship between wind stress curl/divergence and crosswind/downwind SST gradients are no longer linear nor quasi-linear, and the magnitudes of wind stress curl/divergence become much greater. The wind stress field is argued to be significantly affected by both submesoscale SST gradients and surface currents, although the strong surface current curl/divergence turns out to be the dominant drivers of wind stress curl/divergence over the submesoscale eddy and the front. In addition, compared with larger scales, the wind stress curls/divergences introduced by submesoscale surface features are of significantly greater magnitudes than those introduced by the mesoscale eddy and front. The intense response of wind stress to the submesoscale surface features supports their inclusion in modeling the ocean-atmosphere coupled system.

Submesoscale convergence structures and vertical subduction processes are revealed by the contrast tracer experiments. Air-sea turbulent fluxes modeled with the inclusion of surface currents can introduce stronger vertical subduction. The stronger wind stress curl in Exp. A and associated nonlinear Ekman pumping (Stern, 1965) is surmised to be the cause of the stronger vertical transports, with future work needed to verify this inference. Many studies have investigated the strong velocity transports associated with the submesoscale processes (Balwada et al., 2018; D'Asaro et al., 2018; Mahadevan, 2016; Mahadevan et al., 2008; Thomas et al., 2008), but the novel focus of this study is on the intensification of the submesoscale vertical transport due to the inclusion of surface currents in wind stress modeling. Investigation of the impact of this mechanism on the PV distribution reveals that even when less negative PV is injected into the water due to the presence of surface currents in Exp. A, more negative PV is vertically transported into the deep layers of the domain. Thus, the submesoscale-modified wind stress has the potential to change the dynamics in the upper ocean by modifying the PV distribution. Furthermore, although including the surface current in the air-sea turbulent fluxes modeling doesn't rapidly change the magnitudes of wind stress and heat fluxes by much, the potential long-term impacts of the enhancement of wind stress curl/divergence at the submesoscale on mixed-layer heat budget and atmospheric circulation are worth exploring in future works.

Although a limited range of wind speed is investigated and wind-SST interactions (O'Neill et al., 2010; Small et al., 2008) and surface wave mechanisms (Fan et al., 2009; Shi & Bourassa, 2019) are not included in this work, the strong reactions of wind stress and the oceanic submesoscale to each other extends our knowledge of air-sea interaction over the submesoscale regime. This provides insight into how the wind stress field responds to specific submesoscale processes and how these responses potentially influence the evolution of the submesoscale processes. To accurately simulate the wind stress curl/divergence field in the submesoscale regime, including surface current in air-sea turbulent fluxes modeling and using a high-resolution oceanic model with non-hydrostatic module are considered to be necessary. Future studies implementing a fully two-way coupled model are needed to better simulate and understand the feedback between the oceanic submesoscale processes and the atmosphere. This will likely improve the fidelity of long-term climate projections, thereby bettering the principal scientific tool used to investigate climate change.

#### Data Availability Statement

The original MITgcm model outputs are stored in the FSU HPC archive server and the data analysis products and codes leading to this publication was made available as a zenodo repository at <https://zenodo.org/record/6964261%23.YuwSoC%2Dcbyt>. Further inquiries can be directed to the corresponding author.

### Acknowledgments

We thank Tracy Ippolito and Dr. Takaya Uchida for proofreading, Dr. Bruce Cornuelle and the anonymous reviewers for their comments, and Dr. Panagiotis Velissariou for insightful discussion on this work. This research was made possible with the support from Florida State University Research Computing Center for hosting simulations. This material is based upon work supported by the National Science Foundation under Grants OCE-1941963 and OCE-2123632. Any opinions, findings, and conclusions or recommendations expressed in this work are those of the authors and do not necessarily reflect the views of the National Science Foundation.

### References

- Bachman, S. D., Taylor, J. R., Adams, K. A., & Hosegood, P. J. (2017). Mesoscale and submesoscale effects on mixed layer depth in the southern ocean. *Journal of Physical Oceanography*, 47(9), 2173–2188. <https://doi.org/10.1175/JPO-D-17-0034.1>
- Balwada, D., Smith, K. S., & Abernathey, R. (2018). Submesoscale vertical velocities enhance tracer subduction in an idealized Antarctic circumpolar current. *Geophysical Research Letters*, 45(18), 9790–9802. <https://doi.org/10.1029/2018GL079244>
- Benesty, J., Chen, J., Huang, Y., & Cohen, I. (2009). Pearson correlation coefficient. In *Noise reduction in speech processing* (Vol. 2, pp. 37–40). Springer.
- Boccaletti, G., Ferrari, R., & Fox-Kemper, B. (2007). Mixed layer instabilities and restratification. *Journal of Physical Oceanography*, 37(9), 2228–2250. <https://doi.org/10.1175/JPO3101.1>
- Bourassa, M. A., Gille, S. T., Bitz, C., Carlson, D., Cerovecki, I., Clayson, C. A., et al. (2013). High-latitude ocean and sea ice surface fluxes: Challenges for climate research. *Bulletin of the American Meteorological Society*, 94(3), 403–423. <https://doi.org/10.1175/BAMS-D-11-00244.1>
- Branigan, L., Marshall, D. P., Naveira-Garabato, A., & George Nurser, A. J. (2015). The seasonal cycle of submesoscale flows. *Ocean Modelling*, 92, 69–84. <https://doi.org/10.1016/j.ocemod.2015.05.002>
- Branigan, L., Marshall, D. P., Naveira Garabato, A. C., Nurser, A. J. G., & Kaiser, J. (2017). Submesoscale instabilities in mesoscale eddies. *Journal of Physical Oceanography*, 47(12), 3061–3085. <https://doi.org/10.1175/JPO-D-16-0178.1>
- Capet, X., McWilliams, J. C., Molemaker, M. J., & Schepetkin, A. F. (2008). Mesoscale to submesoscale transition in the California current system. Part I: Flow structure, eddy flux, and observational tests. *Journal of Physical Oceanography*, 38(1), 29–43. <https://doi.org/10.1175/2007JPO3671.1>
- Charney, J. G. (1971). Geostrophic turbulence. *Journal of the Atmospheric Sciences*, 28(6), 1087–1095. [https://doi.org/10.1175/1520-0469\(1971\)028<1087:gt>2.0.co;2](https://doi.org/10.1175/1520-0469(1971)028<1087:gt>2.0.co;2)
- Chelton, D. B., Schlax, M. G., Freilich, M. H., & Milliff, R. (2004). Satellite measurements reveal persistent small-scale features in ocean winds. *Science*, 303(5660), 978–983. <https://doi.org/10.1126/science.1091901>
- D'Asaro, E., Lee, C., Rainville, L., Harcourt, R., & Thomas, L. (2011). Enhanced turbulence and energy dissipation at ocean fronts. *Science*, 332(6027), 318–322. <https://doi.org/10.1126/science.1201515>
- D'Asaro, E. A., Shcherbina, A. Y., Klymak, J. M., Molemaker, J., Novelli, G., Guigand, C. M., et al. (2018). Ocean convergence and the dispersion of flotsam. *Proceedings of the National Academy of Sciences*, 115(6), 1162–1167. <https://doi.org/10.1073/pnas.1718453115>
- Dawe, J. T., & Thompson, L. (2006). Effect of ocean surface currents on wind stress, heat flux, and wind power input to the ocean. *Geophysical Research Letters*, 33(9), L09604. <https://doi.org/10.1029/2006GL025784>
- Deremble, B., Wienders, N., & Dewar, W. K. (2013). CheapAML: A simple, atmospheric boundary layer model for use in ocean-only model calculations. *Monthly Weather Review*, 141(2), 809–821. <https://doi.org/10.1175/MWR-D-11-00254.1>
- Dewar, W. K., & Flierl, G. R. (1987). Some effects of the wind on rings. *Journal of Physical Oceanography*, 17(10), 1653–1667. [https://doi.org/10.1175/1520-0485\(1987\)017<1653:seotwo>2.0.co;2](https://doi.org/10.1175/1520-0485(1987)017<1653:seotwo>2.0.co;2)
- Dong, J., Fox-Kemper, B., Zhang, H., & Dong, C. (2020). The scale of submesoscale baroclinic instability globally. *Journal of Physical Oceanography*, 50(9), 2649–2667. <https://doi.org/10.1175/JPO-D-20-0043.1>
- Duhaut, T. H. A., & Straub, D. N. (2006). Wind stress dependence on ocean surface velocity: Implications for mechanical energy input to ocean circulation. *Journal of Physical Oceanography*, 36(2), 202–211. <https://doi.org/10.1175/JPO2842.1>
- Fairall, C. W., Bradley, E. F., Hare, J. E., Grachev, A. A., & Edson, J. B. (2003). Bulk parameterization of air–sea fluxes: Updates and verification for the COARE algorithm. *Journal of Climate*, 16(4), 21–591. [https://doi.org/10.1175/1520-0442\(2003\)016<0571:bpoasf>2.0.co;2](https://doi.org/10.1175/1520-0442(2003)016<0571:bpoasf>2.0.co;2)
- Fan, Y., Ginis, I., & Hara, T. (2009). The effect of wind–wave–current interaction on air–sea momentum fluxes and ocean response in tropical cyclones. *Journal of Physical Oceanography*, 39(4), 1019–1034. <https://doi.org/10.1175/2008JPO4066.1>
- Fox-Kemper, B., Ferrari, R., & Hallberg, R. (2008). Parameterization of mixed layer eddies. Part I: Theory and diagnosis. *Journal of Physical Oceanography*, 38(6), 1145–1165. <https://doi.org/10.1175/2007JPO3792.1>
- Gaube, P., Chelton, D. B., Samelson, R. M., Schlax, M. G., & O'Neill, L. W. (2015). Satellite observations of mesoscale eddy-induced Ekman pumping. *Journal of Physical Oceanography*, 45(1), 104–132. <https://doi.org/10.1175/JPO-D-14-0032.1>
- Gopalakrishnan, G., Cornuelle, B. D., & Hoteit, I. (2013). Adjoint sensitivity studies of loop current and eddy shedding in the Gulf of Mexico. *Journal of Geophysical Research: Oceans*, 118(7), 3315–3335. <https://doi.org/10.1002/jgrc.20240>
- Gopalakrishnan, G., Cornuelle, B. D., Hoteit, I., Rudnick, D. L., & Owens, W. B. (2013). State estimates and forecasts of the loop current in the Gulf of Mexico using the MITgcm and its adjoint: State estimates and Forecasts in the GoM. *Journal of Geophysical Research: Oceans*, 118(7), 3292–3314. <https://doi.org/10.1002/jgrc.20239>
- Hamlington, P. E., Van Roekel, L. P., Fox-Kemper, B., Julien, K., & Chini, G. P. (2014). Langmuir–submesoscale interactions: Descriptive analysis of multiscale frontal spindown simulations. *Journal of Physical Oceanography*, 44(9), 2249–2272. <https://doi.org/10.1175/JPO-D-13-0139.1>
- Hayes, S. P., McPhaden, M. J., & Wallace, J. M. (1989). The influence of sea-surface temperature on surface wind in the eastern equatorial Pacific: Seasonal and interannual variability. *Journal of Climate*, 2(12), 1492–1499. [https://doi.org/10.1175/1520-0442\(1989\)002<1492:tiosst>2.0.co;2](https://doi.org/10.1175/1520-0442(1989)002<1492:tiosst>2.0.co;2)
- Hoskins, B. J. (1974). The role of potential vorticity in symmetric stability and instability. *Quarterly Journal of the Royal Meteorological Society*, 100(425), 480–482. <https://doi.org/10.1002/qj.49710042520>
- Kara, A. B., Rochford, P. A., & Hurlburt, H. E. (2000). Efficient and accurate bulk parameterizations of air–sea fluxes for use in general circulation models. *Journal of Atmospheric Oceanic Technology*, 17(10), 18–1438. [https://doi.org/10.1175/1520-0426\(2000\)017<1421:eaabpo>2.0.co;2](https://doi.org/10.1175/1520-0426(2000)017<1421:eaabpo>2.0.co;2)
- Klein, P., & Lapeyre, G. (2009). The oceanic vertical pump induced by mesoscale and submesoscale turbulence. *Annual Review of Marine Science*, 1, 351–375. <https://doi.org/10.1146/annurev.marine.010908.163704>
- Köhn, E. E., Thomsen, S., Arévalo-Martínez, D. L., & Kanzow, T. (2017). Submesoscale CO<sub>2</sub> variability across an upwelling front off Peru. *Ocean Science*, 13(6), 1017–1033. <https://doi.org/10.5194/os-13-1017-2017>
- Lee, T., Waliser, D. E., Li, J.-L. F., Landerer, F. W., & Gierach, M. M. (2013). Evaluation of CMIP3 and CMIP5 wind stress climatology using satellite measurements and atmospheric reanalysis products. *Journal of Climate*, 26(16), 5810–5826. <https://doi.org/10.1175/JCLI-D-12-00591.1>
- Lévy, M., Ferrari, R., Franks, P. J. S., Martin, A. P., & Rivière, P. (2012). Bringing physics to life at the submesoscale: Frontier. *Geophysical Research Letters*, 39(14). <https://doi.org/10.1029/2012GL052756>
- Lévy, M., Franks, P. J. S., & Smith, K. S. (2018). The role of submesoscale currents in structuring marine ecosystems. *Nature Communications*, 9(1), 4758. <https://doi.org/10.1038/s41467-018-07059-3>
- Lévy, M., Lovino, D., Resplandy, L., Klein, P., Madec, G., Treguiet, A., et al. (2012). Large-scale impacts of submesoscale dynamics on phytoplankton: Local and remote effects. *Ocean Modelling*, 43–44, 77–93. <https://doi.org/10.1016/j.ocemod.2011.12.003>
- Lindzen, R. S., & Nigam, S. (1987). On the role of sea surface temperature gradients in forcing low-level winds and convergence in the tropics. *Journal of the Atmospheric Sciences*, 44(17), 2418–2436. [https://doi.org/10.1175/1520-0469\(1987\)044<2418:OTROSS>2.0.CO;2](https://doi.org/10.1175/1520-0469(1987)044<2418:OTROSS>2.0.CO;2)

- Ma, X., Jing, Z., Chang, P., Liu, X., Montuoro, R., Small, R. J., et al. (2016). Western boundary currents regulated by interaction between ocean eddies and the atmosphere. *Nature*, 535(7613), 533–537. <https://doi.org/10.1038/nature18640>
- Mahadevan, A. (2016). The impact of submesoscale physics on primary productivity of plankton. *Annual Review of Marine Science*, 8(1), 161–184. <https://doi.org/10.1146/annurev-marine-010814-015912>
- Mahadevan, A., Thomas, L. N., & Tandon, A. (2008). Comment on “eddy/wind interactions stimulate extraordinary mid-ocean plankton blooms”. *Science*, 320(5875), 448b. <https://doi.org/10.1126/science.1152111>
- Maloney, E. D., & Chelton, D. B. (2006). An assessment of the sea surface temperature influence on surface wind stress in numerical weather prediction and climate models. *Journal of Climate*, 19(12), 2743–2762. <https://doi.org/10.1175/JCLI3728.1>
- Marshall, J., Hill, C., Perelman, L., & Adcroft, A. (1997). Hydrostatic, quasi-hydrostatic, and nonhydrostatic ocean modeling. *Journal of Geophysical Research*, 102(C3), 5733–5752. <https://doi.org/10.1029/96JC02776>
- Marshall, J., & Nurser, A. J. G. (1992). Fluid dynamics of oceanic thermocline ventilation. *Journal of Physical Oceanography*, 22(6), 583–595. [https://doi.org/10.1175/1520-0485\(1992\)022<0583:FDOOTV>2.0.CO;2](https://doi.org/10.1175/1520-0485(1992)022<0583:FDOOTV>2.0.CO;2)
- McGillicuddy, D. J., Jr., Anderson, L. A., Doney, S. C., & Maltrud, M. E. (2003). Eddy-driven sources and sinks of nutrients in the upper ocean: Results from a 0.1° resolution model of the North Atlantic. *Global Biogeochemical Cycles*, 17(2), 1035. <https://doi.org/10.1029/2002gb001987>
- McWilliams, J. C. (2003). *Diagnostic force balance and its limits, in nonlinear processes in geophysical fluid dynamics* (pp. 287–304). Kluwer Academic Publishers.
- McWilliams, J. C. (2016). Submesoscale currents in the ocean. *Proceedings of the Royal Society A: Mathematical, Physical and Engineering Sciences*, 472(2189), 20160117. <https://doi.org/10.1098/rspa.2016.0117>
- McWilliams, J. C., Molemaker, M. J., & Yavneh, I. (2001). From stirring to mixing of momentum: Cascades from balanced flows to dissipation in the oceanic interior. In *Near-boundary processes and their parameterization: Proceedings of the 'Aha Huliko'a Hawaiian winter workshop, Honolulu, HI* (pp. 59–66). University of Hawaii at Manoa.
- Moore, G. W. K., & Renfrew, I. A. (2002). An assessment of the surface turbulent heat fluxes from the NCEP–NCAR reanalysis over the western boundary currents. *Journal of Climate*, 15, 18–2037. [https://doi.org/10.1175/1520-0442\(2002\)015<2020:aaotst>2.0.co;2](https://doi.org/10.1175/1520-0442(2002)015<2020:aaotst>2.0.co;2)
- O'Neill, L. W., Esbensen, S. K., Thum, N., Samelson, R. M., & Chelton, D. B. (2010). Dynamical analysis of the boundary layer and surface wind responses to mesoscale SST perturbations. *Journal of Climate*, 23(3), 559–581. <https://doi.org/10.1175/2009JCLI2662.1>
- Raschle, N., Chapron, B., Molemaker, J., Nogueira, F., Ocampo-Torres, F. J., Osuna Canedo, J. P., et al. (2020). Monitoring intense oceanic fronts using sea surface roughness: Satellite, airplane, and in situ comparison. *Journal of Geophysical Research: Oceans*, 125(8), e2019JC015704. <https://doi.org/10.1029/2019JC015704>
- Renault, L., Masson, S., Arsouze, T., Madec, G., & McWilliams, J. C. (2020). Recipes for how to force oceanic model dynamics. *Journal of Advances in Modeling Earth Systems*, 12(2), e2019MS001715. <https://doi.org/10.1029/2019MS001715>
- Renault, L., McWilliams, J. C., & Gula, J. (2018). Dampening of submesoscale currents by air-sea stress coupling in the Californian upwelling system. *Scientific Reports*, 8(1), 13388. <https://doi.org/10.1038/s41598-018-31602-3>
- Renault, L., McWilliams, J. C., & Masson, S. (2017). Satellite observations of imprint of oceanic current on wind stress by air-sea coupling. *Scientific Reports*, 7(1), 17747. <https://doi.org/10.1038/s41598-017-17939-1>
- Renault, L., McWilliams, J. C., & Penven, P. (2017). Modulation of the Agulhas current retroflection and leakage by oceanic current interaction with the atmosphere in coupled simulations. *Journal of Physical Oceanography*, 47(8), 2077–2100. <https://doi.org/10.1175/JPO-D-16-0168.1>
- Renault, L., Molemaker, M. J., Gula, J., Masson, S., & McWilliams, J. C. (2016). Control and stabilization of the Gulf stream by oceanic current interaction with the atmosphere. *Journal of Physical Oceanography*, 46(11), 3439–3453. <https://doi.org/10.1175/JPO-D-16-0115.1>
- Renault, L., Molemaker, M. J., McWilliams, J. C., Shchepetkin, A. F., Lemarié, F., Chelton, D., et al. (2016). Modulation of wind work by oceanic current interaction with the atmosphere. *Journal of Physical Oceanography*, 46(6), 1685–1704. <https://doi.org/10.1175/JPO-D-15-0232.1>
- Roberts, J. B., Robertson, F. R., Clayton, C. A., & Bosilovich, M. G. (2012). Characterization of turbulent latent and sensible heat flux exchange between the atmosphere and ocean in MERRA. *Journal of Climate*, 25(3), 821–838. <https://doi.org/10.1175/JCLI-D-11-00029.1>
- Rogers, D. P. (1995). Air-sea interaction: Connecting the ocean and atmosphere. *Reviews of Geophysics*, 33(S2), 1377–1383. <https://doi.org/10.1029/95RG00255>
- Rosso, I., Hogg, A. M. C., Kiss, A. E., & Gayen, B. (2015). Topographic influence on submesoscale dynamics in the Southern Ocean. *Geophysical Research Letters*, 42(4), 1139–1147. <https://doi.org/10.1002/2014GL062720>
- Sabine, C., & Tanhua, T. (2010). Estimation of anthropogenic CO<sub>2</sub> inventories in the ocean. *Annual Review of Marine Science*, 2(1), 175–198. <https://doi.org/10.1146/annurev-marine-120308-080947>
- Sarmiento, J. L., Orr, J. C., & Siegenthaler, U. (1992). A perturbation simulation of CO<sub>2</sub> uptake in an ocean general circulation model. *Journal of Geophysical Research*, 97(C3), 3621–3645. <https://doi.org/10.1029/91JC02849>
- Scott, R. B., & Arbic, B. K. (2007). Spectral energy fluxes in geostrophic turbulence: Implications for ocean energetics. *Journal of Physical Oceanography*, 37(3), 673–688. <https://doi.org/10.1175/JPO3027.1>
- Seo, H. (2017). Distinct influence of air–sea interactions mediated by mesoscale sea surface temperature and surface current in the Arabian Sea. *Journal of Climate*, 30(20), 8061–8080. <https://doi.org/10.1175/JCLI-D-16-0834.1>
- Seo, H., Miller, A. J., & Norris, J. R. (2016). Eddy–wind interaction in the California Current System: Dynamics and impacts. *Journal of Physical Oceanography*, 46(2), 439–459. <https://doi.org/10.1175/JPO-D-15-0086.1>
- Seo, H., Subramanian, A. C., Song, H., & Chowdary, J. S. (2019). Coupled effects of ocean current on wind stress in the Bay of Bengal: Eddy energetics and upper ocean stratification. *Deep Sea Research Part II: Topical Studies in Oceanography*, 168, 104617. <https://doi.org/10.1016/j.dsr2.2019.07.005>
- Shi, Q., & Bourassa, M. A. (2019). Coupling ocean currents and waves with wind stress over the Gulf stream. *Remote Sensing*, 11(12), 1476. <https://doi.org/10.3390/rs11121476>
- Small, R. J., de Szoeke, S., Xie, S., O'Neill, L., Seo, H., Song, Q., et al. (2008). Air–sea interaction over ocean fronts and eddies. *Dynamics of Atmospheres and Oceans*, 45(3–4), 274–319. <https://doi.org/10.1016/j.dynatmoce.2008.01.001>
- Smith, S. D. (1988). Coefficients for sea surface wind stress, heat flux, and wind profiles as a function of wind speed and temperature. *Journal of Geophysical Research*, 93(C12), 15467–15472. <https://doi.org/10.1029/JC093iC12p15467>
- Spall, M. A. (2007). Midlatitude wind stress–sea surface temperature coupling in the vicinity of oceanic fronts. *Journal of Climate*, 20(15), 3785–3801. <https://doi.org/10.1175/JCLI4234.1>
- Stamper, M. A., & Taylor, J. R. (2017). The transition from symmetric to baroclinic instability in the Eady model. *Ocean Dynamics*, 67(1), 65–80. <https://doi.org/10.1007/s10236-016-1011-6>
- Stern, M. (1965). Interaction of a uniform wind stress with a geostrophic vortex. *Deep-Sea Research and Oceanographic Abstracts*, 12(3), 355–367. [https://doi.org/10.1016/0011-7471\(65\)90007-0](https://doi.org/10.1016/0011-7471(65)90007-0)



- Stone, P. (1966). On non-geostrophic baroclinic stability. *Journal of the Atmospheric Sciences*, 23(4), 390–400. [https://doi.org/10.1175/1520-0469\(1966\)023<0390:ongbs>2.0.co;2](https://doi.org/10.1175/1520-0469(1966)023<0390:ongbs>2.0.co;2)
- Strobach, E., Klein, P., Molod, A., Fahad, A. A., Trayanov, A., Menemenlis, D., & Torres, H. (2022). Local air–sea interactions at ocean mesoscale and submesoscale in a western boundary current. *Geophysical Research Letters*, 49(7), e2021GL097003. <https://doi.org/10.1029/2021GL097003>
- Su, Z., Wang, J., Klein, P., Thompson, A. F., & Menemenlis, D. (2018). Ocean submesoscales as a key component of the global heat budget. *Nature Communications*, 9(1), 775. <https://doi.org/10.1038/s41467-018-02983-w>
- Sullivan, P. P., McWilliams, J. C., Weil, J. C., Patton, E. G., & Fernando, H. J. S. (2020). Marine boundary layers above heterogeneous SST: Across-front winds. *Journal of the Atmospheric Sciences*, 77(12), 4251–4275. <https://doi.org/10.1175/JAS-D-20-0062.1>
- Thomas, L., & Ferrari, R. (2008). Friction, frontogenesis, and the stratification of the surface mixed layer. *Journal of Physical Oceanography*, 38(11), 2501–2518. <https://doi.org/10.1175/2008JPO3797.1>
- Thomas, L. N. (2008). Formation of intrathermocline eddies at ocean fronts by wind-driven destruction of potential vorticity. *Dynamics of Atmospheres and Oceans*, 45(3–4), 252–273. <https://doi.org/10.1016/j.dynatmoce.2008.02.002>
- Thomas, L. N., & Lee, C. M. (2005). Intensification of ocean fronts by down-front winds. *Journal of Physical Oceanography*, 35(6), 1086–1102. <https://doi.org/10.1175/JPO2737.1>
- Thomas, L. N., Tandon, A., & Mahadevan, A. (2008). Submesoscale processes and dynamics. In M. W. Hecht & H. Hasumi (Eds.), *Geophysical monograph series* (Vol. 177, pp. 17–38). American Geophysical Union.
- Wallace, J. M., Mitchell, T. P., & Deser, C. (1989). The influence of sea-surface temperature on surface wind in the eastern equatorial Pacific: Seasonal and interannual variability. *Journal of Climate*, 2(12), 1492–1499. [https://doi.org/10.1175/1520-0442\(1989\)002<1492:TIOSST>2.0.CO;2](https://doi.org/10.1175/1520-0442(1989)002<1492:TIOSST>2.0.CO;2)
- Wenegrat, J. O., Thomas, L. N., Gula, J., & McWilliams, J. C. (2018). Effects of the submesoscale on the potential vorticity budget of ocean mode waters. *Journal of Physical Oceanography*, 48(9), 2141–2165. <https://doi.org/10.1175/JPO-D-17-0219.1>
- Wu, Y., Zhai, X., & Wang, Z. (2017). Decadal-mean impact of including ocean surface currents in bulk formulas on surface air–sea fluxes and ocean general circulation. *Journal of Climate*, 30(23), 9511–9525. <https://doi.org/10.1175/JCLI-D-17-0001.1>
- Zhai, X., & Greatbatch, R. J. (2007). Wind work in a model of the northwest Atlantic Ocean. *Geophysical Research Letters*, 34(4), L04606. <https://doi.org/10.1029/2006GL028907>
- Zhang, D., Cronin, M. F., Wen, C., Xue, Y., Kumar, A., & McClurg, D. (2016). Assessing surface heat fluxes in atmospheric reanalyses with a decade of data from the NOAA Kuroshio extension observatory: Reanalysis heat flux and KEO observation. *Journal of Geophysical Research: Oceans*, 121(9), 6874–6890. <https://doi.org/10.1002/2016JC011905>
- Zhou, H., Dewar, W., Yang, W., Liu, H., Chen, X., Li, R., et al. (2022). Observations and modeling of symmetric instability in the ocean interior in the Northwestern Equatorial Pacific. *Communications Earth & Environment*, 3(1), 28. <https://doi.org/10.1038/s43247-022-00362-4>